ELSEVIER

Contents lists available at ScienceDirect

# **Materials Characterization**

journal homepage: www.elsevier.com/locate/matchar





# Quantitative measurement of corrosion at the nanoscale by *in situ* spectral modulation interferometry

Ebenezer O. Fanijo <sup>a,\*,1</sup>, Joseph G. Thomas <sup>b,1</sup>, Yizheng Zhu <sup>b</sup>, Javier Esquivel Guerrero <sup>c</sup>, Niamh C. Hosking <sup>c</sup>, Wenjun Cai <sup>d</sup>, F. Marc Michel <sup>e</sup>, Alexander S. Brand <sup>a,d,\*</sup>

- <sup>a</sup> The Charles E. Via, Jr. Department of Civil and Environmental Engineering, Virginia Polytechnic Institute and State University, USA
- <sup>b</sup> Department of Electrical and Computer Engineering, Virginia Polytechnic Institute and State University, USA
- <sup>c</sup> Ford Motor Company, USA
- <sup>d</sup> Department of Material Science and Engineering, Virginia Polytechnic Institute and State University, USA
- e Department of Geosciences, Virginia Polytechnic Institute and State University, USA

#### ARTICLE INFO

# Keywords: Spectral modulation interferometry Quantitative phase imaging Pitting corrosion Corrosion rate Rate spectra

#### ABSTRACT

This research study presents a novel application of a quantitative phase microscopy technique, spectral modulation interferometry (SMI), for in situ nanoscale characterization of corrosion of an aluminum alloy in real time. SMI offers high sensitivity, rapid image acquisition, and speckle-free images; thus, real-time quantification of surface topography evolution during corrosion can be obtained accurately to evaluate the temporally- and spatially-dependent corrosion rates. With an innovative additive-manufactured fluid cell, experiments were performed in situ under flowing solution conditions. Electrochemical tests via stepwise polarization and solution chemistry through collected aliquots of outflow solution were also performed alongside the nanoscale SMI experiment to simultaneously provide a corroborating corrosion rate measurement. Based on the quantitative 3D height profiles across the corroded surface, pit formation resulting from rapid local corrosion was predominant, appearing at different times and are heterogeneously distributed across the surface. The computed timedependent dissolution rates of aluminum also varied as the experiment proceeded, with the combination of linear and nonlinear surface normal distributions. An initial mean linear dissolution rate of  $[0.40\pm0.007]~\mu mol$  $m^{-2}$  s<sup>-1</sup> transitioned to a more rapid mean rate of [1.95  $\pm$  0.035]  $\mu$ mol m<sup>-2</sup> s<sup>-1</sup>, driven by the anodic polarization. Dissolution rates from the three performed methods follow similar trends and there is the visibility of linking the nanoscale in situ SMI data to the electrochemical corrosion measurements and ex situ chemical solution analysis. At the end of the corrosion period, rates of 118  $\mu$ mol m<sup>-2</sup> s<sup>-1</sup>, 71  $\mu$ mol m<sup>-2</sup> s<sup>-1</sup>, and 2.45  $\mu$ mol m<sup>-2</sup> s<sup>-1</sup> were obtained from electrochemical measurements, ex situ solution analyses, and in situ SMI corrosion measurement, respectively. Finally, these experimental results validate the applicability of SMI for in situ nanoscale characterization of a corroding alloy surface.

# 1. Introduction

Corrosion is the main cause of the deterioration of metallic materials, and it has since received great attention both in academic and in applied industrial studies from the literature [1–7]. Localized corrosion, like pitting and intergranular corrosion (IGC) are the corrosion modes that commonly cause metallic degradation in aggressive environments (e.g., chloride-containing environments) [8–10]. It is also concluded that economic losses associated with metallic structure corrosion exceed 3%

of the gross domestic product in developed countries and more than 7% of the undeveloped countries [11,12]. A 2016 report indicated that the global cost of corrosion was \$2.5 trillion [13]. As a result, the understanding of the corrosion mechanism(s) and kinetics at the micro- and nanoscale in relation to their microstructure and the environment are critical to understanding the macroscopic behavior. Of interest, AA6111 is extensively utilized as a wrought sheet in various industrial applications, such as automotive, marine, architectural, and aerospace [14–16], due to the combination of high strength and good formability in the

E-mail addresses: ebenfanijo@vt.edu (E.O. Fanijo), jgt97@vt.edu (J.G. Thomas), yizhu1@vt.edu (Y. Zhu), jesqui22@ford.com (J. Esquivel Guerrero), nhoskin5@ford.com (N.C. Hosking), caiwd@vt.edu (W. Cai), mfrede2@vt.edu (F.M. Michel), asbrand@vt.edu (A.S. Brand).

 $<sup>^{\</sup>ast}$  Corresponding author.

<sup>&</sup>lt;sup>1</sup> These authors contributed equally to this study

solutionized and naturally aged conditions [17,18]. In recent years, applications of different characterization techniques and data processing methods to investigate nanoscale corrosion mechanism(s) and kinetics of metallic corrosion has grown substantially, such as optical microscopy (OM), X-ray diffraction (XRD), and scanning electron microscopy (SEM) [19–24]; transmission electron microscopy (TEM) [25]; in situ liquid TEM [26,27]; X-ray computed tomography [28–31]; atomic force microscopy (AFM), scanning Kelvin probe force microscopy (SKPFM), and electrochemical atomic force microscopy (EC-AFM) [32–37]; vertical scanning interferometry (VSI) [38–40]; and digital holography and digital holographic microscopy (DHM) [9,10,41–48].

Optical probe quantitative phase microscopy (QPM) methods, such as VSI and DHM, are capable of generating high-resolution 3D surface topography data and computing rate kinetics based on changes in the surface profile over time. These methods also have such advantages as high axial resolution, full-field view, nondestructive observation, contact-free high sensitivity, and fast response [49,50]. Taking inspiration from the geochemistry literature, the use of micro- and nanoscale surface topography measurements have proven to be particularly powerful [51], such as using VSI [52-61] and DHM [62-68] to quantify dissolution kinetics. With the use of in situ DHM, it is possible to observe rapid kinetic nanoscale events that may otherwise be missed by other ex situ methods [63,64,67,68]. Indeed, corrosion and electrochemical science studies have also begun to implement such optical interferometric techniques [9,10,38-42,44-48,69-74]. Recently, Asgari et al. [42] used reflective DHM for quantitative evaluation of microstructural corrosion in austenitic stainless steel and was able to distinguish between intergranular and transgranular corrosion. Pedram et al. [10] employed reflective DHM to investigate the growth of pitting corrosion of a custom 450 alloy and they reported that it was possible to predict pit initiation and growth.

While these optical techniques have been explored for dissolution and corrosion studies, there is still a lack of high-quality quantitative kinetic data that would derive fundamental mechanisms of metallic corrosion at the micro- and nanoscales. Furthermore, previous corrosion studies only focused on using *ex situ* VSI [38–40,75,76] and *ex situ* DHM [9,10,41,45,46,77], which offers a significant opportunity to develop an *in situ* QPM approach in corrosion science. While Abbot *et al.* [69] used *in situ* DHM to quantify electrodeposition rates, no study has yet used QPM to evaluate *in situ* corrosion rates.

This study presents a novel application of a QPM approach, spectral modulation interferometry (SMI), to *in situ* corrosion studies. SMI combines spectral-domain low-coherence interferometry with a spectral modulation technique [78] and offers speckle-free imaging and an order of magnitude better sensitivity and speed than DHM. The SMI provides surface topography data with sub-micron lateral resolution and sub-nanometer vertical precision. This approach is applied for *in situ* imaging of nanoscale surface topography evolution of an aluminum alloy surface in aqueous solutions. A potentiostat is connected simultaneously to apply electrochemical techniques (In this case, stepwise polarization), while the SMI serves as a powerful visual to help us interpret the electrochemical response. Lastly, solution composition is evaluated to provide a third corrosion measurement. This innovative approach thus presents a spatial and temporal scale of *in situ* corrosion in real time that is rarely explored in the literature.

#### 2. Experimental methodology

#### 2.1. Materials

This study applies SMI to study the *in situ* nanoscale corrosion for an AA6111-T4 aluminum alloy (Fig. 2). The nominal chemical composition of a typical AA6111 is shown in Table 1.

Samples were cut to dimensions of 1.25 cm by 1.25 cm by 0.5 cm and mounted in epoxy. The unexposed side of each sample was then electrically connected to a copper wire. The visible side was consecutively ground from #320 grit (33  $\mu m)$  to #4000 grit (5  $\mu m)$  using silicon carbide (SiC) papers, and subsequent polishing was conducted with 3  $\mu m$  and 1  $\mu m$  diamond paste. Final polishing was performed with a vibratory polisher in an aqueous suspension of 0.02  $\mu m$  colloidal silica (pH  $\sim 10.5$ ). Finally, the samples were cleaned with alcohol and double-distilled water for three minutes in an ultrasonic bath as shown in Fig. 2. This polishing was necessary to provide a surface of suitable smoothness to be imaged by SMI (i.e., a required surface roughness value of <100 nm).

#### 2.2. Spectral modulation interferometry

SMI was developed by Zhu and colleagues [78], based on spectral-domain interferometry, has high optical pathlength (OPL) sensitivity, has high acquisition speed (up to 120 Hz), and has sub-nanometer vertical and sub-micrometer lateral resolution. Fig. 2 illustrates the schematic SMI setup and the principle behind the technique for phase imaging. While its signal is generated in spectral domain in contrast to DHM's spatial domain, the signal model and processing procedure in SMI is similar to off-axis DHM techniques. However, its dispersive and confocal imaging scheme eliminates laser speckle, producing speckle-free coherent images with high phase sensitivity and imaging rate.

As shown in Fig. 2, SMI uses broadband, spatially-coherent light from a superluminescent diode (SLD, Superlum;  $\lambda=837$  nm,  $\Delta\lambda=54$  nm) coupled into a single-mode fiber. A 50/50 fiber coupler directs light into the system, where it is launched into the free-space optical path via a collimating lens. A 1D galvo-scanner (x-direction) scans the collimated beam in one dimension, while a transmission grating (Wasatch Photonics; 600 mm $^{-1}$ ) disperses the beam into propagation angles varying by wavelength (y-direction). The dispersed beam is then focused by the microscope objectives in the form of a wavelength dispersed line, similar to other forms of spectrally-encoded imaging [80–83], and the galvo scanner scans the line over the sample to build up two-dimensional images.

The reflected beams from the sample and reference mirrors are backpropagated through the system and directed to the spectrometer by the fiber coupler. The interference spectrums are then recorded by the custom spectrometer with a line scan camera (e2v; EM1, 1024-pixel, maximum line rate 78 kHz). Afterward, the recorded interference patterns are subjected to numerical processing by a Fourier transform. The processing steps have been earlier discussed in detail in the development of SMI [78]. After reconstruction, each interferogram produces an amplitude-contrast image (similar to a typical optical microscope image in reflection mode) and a phase-contrast image that contains surface height information. Eq. (4) shows SMI's signal model for estimating sample surface heights. The interference intensity I(x, y) recorded by the spectrometer is modulated by the sample phase  $\phi_s(x, y)$  obtained from the optical interference of complex sample amplitude  $E_s$  (x, y) and reference amplitude  $E_r(x, y)$ .  $L_0$  is the initial OPL offset of the Linnik interferometer ( $L_0 = L_s - L_r$ ),  $k_0$  is the starting wavenumber, and  $\alpha$  (in rad

Table 1
Typical AA6111 nominal chemical composition ranges (wt%) [79].

Al	Si	Fe	Cu	Mn	Mg	Cr	Zn	Ti
Bal.	0.60-1.10	< 0.40	0.50-0.90	0.10-0.45	0.50-1.00	< 0.10	< 0.15	< 0.10

 ${\rm m}^{-2}$ ) is the dispersion coefficient of grating-diffracted beams. Sample surface height information is contained in the phase term  $\phi_s$  (x, y). In this configuration, variations in phase information on the sample due to the corrosion process as a function of time can be obtained. That is, different optical paths originate from the different depths of pits (arising from corrosion), producing delays in the optical phase which, according to Eq. (4), produce distinct changes in the detected optical interference pattern.

$$I(x,) = \frac{E_r}{2} + \frac{I(x,y)}{2} + 2E_r E_s(x,y)cos(2k_0L_0 + 2\alpha L_0(y) + 2\phi_s(x,y))$$
(4)

While the SMI is capable of acquiring images as rapidly as 120 Hz, the volume of data over a 240 min experiment precludes such a rate due to the time required to process each image. Therefore, this study collected images every 30 s, resulting in a total of 480 images, and analyzed using MATLAB programming software. Prior to image collection, the SMI's interferometer arms used matching Nikon Fluor  $40\times \ 0.80$  W water immersion objectives to image through the solution. In the fluid cell, a 25  $\mu m$  thick polymer film was placed between the objective lens and the solution in order to protect the lens, as shown in Fig. 1c. A drop of distilled water was placed between the objective lens and the protective film in the sample path to provide an optical path equivalent to typical water immersion between the lens and the sample surface. A drop of water was also placed between the objective and mirror in the reference arm to provide a matching optical path.

#### 2.3. Electrochemical fluid cell development

A flow-through fluid cell is necessary to provide the solution conditions for in situ imaging. The flowing solution provides nominally undersaturated conditions, thereby allowing for the study of the corrosion rate without the suspended solids (i.e., insoluble corrosion products) that interfere with imaging quality. The flowing conditions also remove any gas bubbles in the solution produced during the reaction. Similar in concept to the fluid cell used previously by Brand and colleagues [62-66,84], this study utilized a novel additive-manufacturing approach to rapidly prototype various designs. Using the method by Michel and colleagues [85,86], inverse stereolithography was used to additive manufacture the fluid cell. The cell's body was constructed of a chemically inert and electrically insulative methacrylated polymer. The cell design accommodated the SMI objective lens and the three electrodes: the working electrode (WE), the reference electrode (RE), and the counter electrode (CE), as shown in Fig. 3. The cell also includes inlet and outlet ports for the flowing solution. An injection peristaltic pump was used to produce flowing conditions. Aliquots of solution were collected from the outlet port for solution chemistry analysis using inductively-coupled plasma mass spectroscopy (ICP-MS). A Thermo Electron iCAP-RQ ICP-MS per Standard Method 3125-B was used [87].

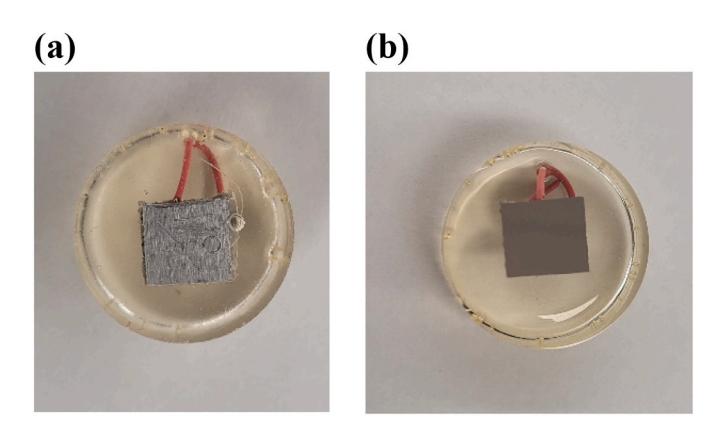


**Fig. 1.** Test samples (AA 6111) sealed with marine epoxy resin for corrosion tests: (a) unpolished sample, and (b) polished sample.

This *in situ* corrosion experiment was performed at a solution flow rate of 40 mL min<sup>-1</sup> through the cell. The flow rate was determined by measuring average corrosion rates as a function of flow rate and the flow rate with the minimal standard error (*i.e.*, better consistency and less variation in the result) was selected; more detail about the flow rate analysis is provided in the Appendix A.

#### 2.4. Electrochemical test

With this selected flow rate, the corrosion measurements were conducted using a three-electrode electrochemical cell: 1) the sample is attached to the anodic pole, acting as the WE; 2) a custom 450 stainless steel strip acting as the CE connected to the cathodic pole; and 3) a silver-silver chloride (Ag/AgCl) as the RE. The CE has an area of  $1.6~{\rm cm}^2$ , which is similar to the WE area. The corrosion experiment was conducted in a  $0.5~{\rm wt}\%$  NaCl solution acidified to pH  $\sim$  2.9 by acetic acid.

The polarization measurement was performed using a Gamry potentiostat Interface 1010E and Gamry ESA400™ (Electrochemical Signal Analyzer) software. The sample was first exposed to the solution and held at the open circuit potential ( $E_{oc}$ ) for 1 h to stabilize the system. Subsequently, a potentiodynamic polarization (PDP) test was performed by applying a potential in the anodic direction within a range of +500 mV above  $E_{oc}$  at a scanning rate of 0.167 mV/s. The applied potential was measured against an Ag/AgCl reference electrode. PDP test was conducted to characterize the corrosion kinetics under anodic polarization. To complement the PDP method, a stepwise potential vs. Ag/ AgCl was applied at 10 mV and held at 15-min intervals. A potential applied in a stepwise manner was chosen in this work rather than the usual potentiodynamic control. This stepwise polarization method allows for a detailed study of the potential-dependent corrosion processes of the alloys in terms of 1) the initiation sites, 2) the extent of dissolution or localized pitting in the matrix of bulk alloy, 3) the level of sensitivity to intermetallic microstructure, and 4) their relations to intergranular corrosion (IGC) [34,88]. The stepwise procedure was continued until the point when the anodic current is significantly too high, wherein either IGC or pitting corrosion as occur.

Aliquots of the outflow solution were collected and evaluated by ICP-MS. The ionic concentrations (such as  $\mathrm{Al}^{3+}$ ) measured from this method will provide a corrosion rate estimate based on the ion dissolving into the solution. In principle, this method is similar to Ogle's in-line corrosion monitoring by inductively coupled plasma atomic emission spectroscopy (ICP-AES) [89,90]. Note that, while ICP-MS can measure a variety of elements in solution, the interest of the study is only limited to Al, as Al corrosion in water at the selected acidic pH forms dissolvable ions ( $\mathrm{Al}^{3+}$ ) per the Pourbaix diagram.

Finally, the microstructural analysis of the sample surface before and after corrosion was also examined using scanning electron microscopy (SEM) and energy-dispersive X-ray spectroscopy (EDS). This surface investigation was also performed to corroborate the morphology observed by SMI.

# 2.5. Corrosion rate calculations

By this experimental configuration, three *simultaneous* measurements of corrosion rate can be conducted: 1) electrochemical test via potentiostatic polarization; 2) solution composition analysis by ICP-MS, based on changes in the Al<sup>3+</sup> concentration; and 3) nanoscale surface topography measurement by SMI, based on changes to the surface height over time. Table 2 lists the rate equations from these three methods, including conversions for equivalent units, where R is the corrosion rate (in mol m<sup>-2</sup> s<sup>-1</sup>); i is the current density (in  $\mu$ A cm<sup>-2</sup>); M is the sample atomic weight (27 g mol<sup>-1</sup>); n is the charge number (e.g., for Al, n = 3); F is the Faraday constant (96,485 s A mol<sup>-1</sup>);  $\rho$  is the sample density (2.71 g cm<sup>-3</sup>);  $K_e$  is a unit conversion factor (0.01 m cm<sup>-1</sup>); f is the solution flow rate (40 mL min<sup>-1</sup>); G are the solution concentrations (in mol L<sup>-1</sup>) of the outflow and inflow, respectively;  $\eta$  is the stoichiometric

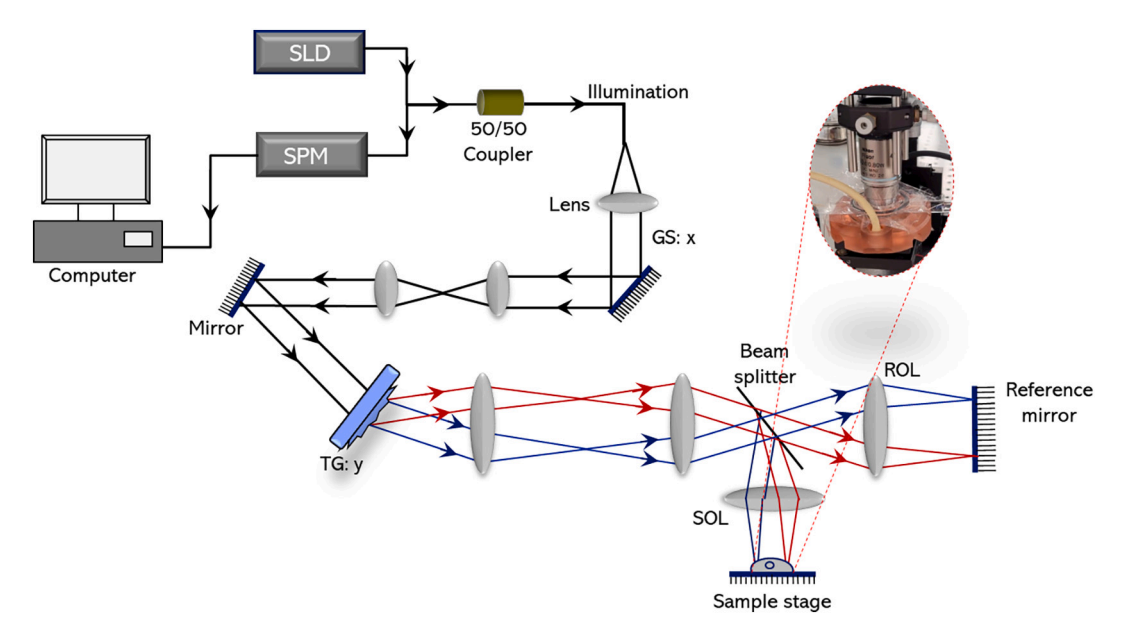


Fig. 2. Schematic setup of SMI techniques for phase imaging. SLD – superluminescent diode, SPM – spectrometer, GS: x – 1D Galvo-scanner (x-direction), TG: y-direction Transmitting grating, ROL – reference objective lens, SOL – sample objective lens.

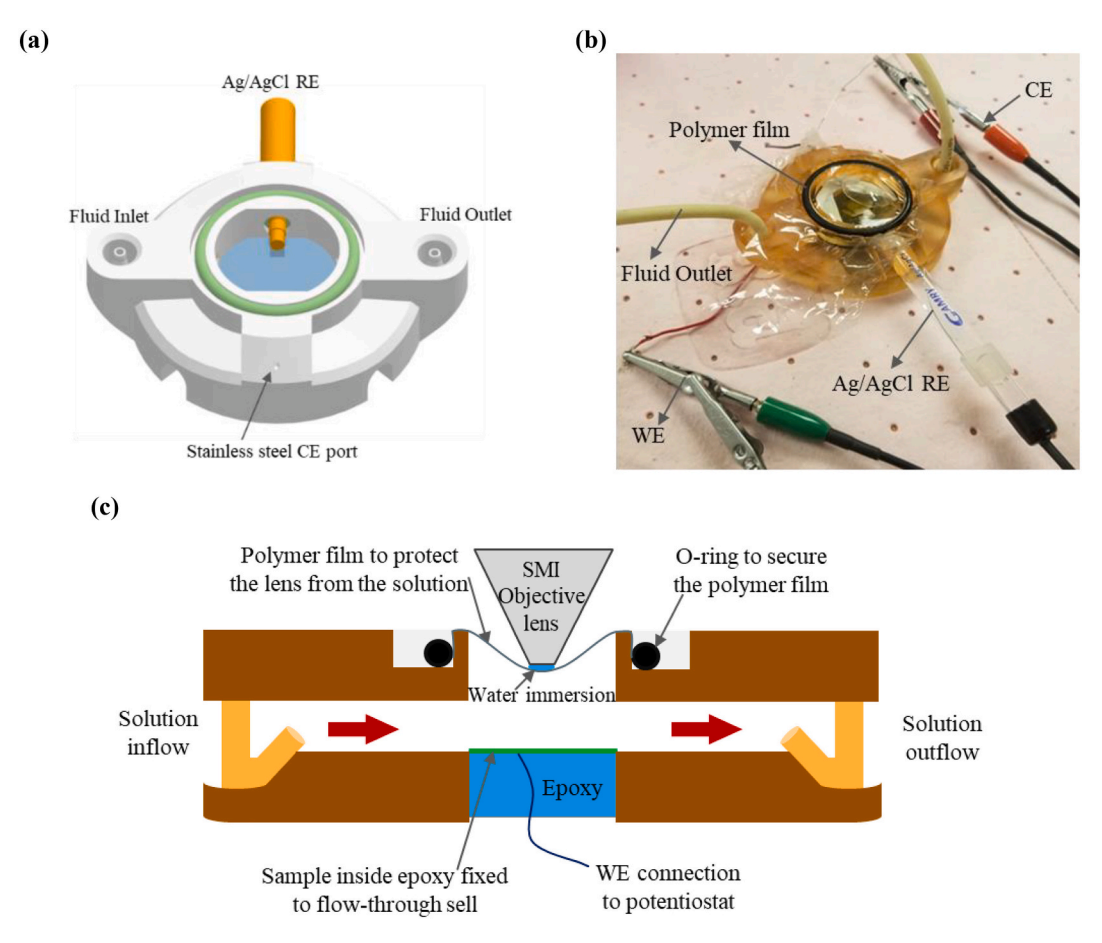


Fig. 3. (a) Design of the flow-through electrochemical fluid cell with designed ports for all the electrodes (WE, CE, RE), fluid inlet and outlet, and space for the SMI objective lens. (b) A typical setup with the cell connected to the electrodes and SMI objective lens will fit in the open space on the top of the cell. (c) Cross-section schematic of the cell.

coefficient of the element (e.g., for Al,  $\eta=3$ );  $K_c$  is the unit conversion factor for solution composition  $(1.67\times 10^5~{\rm cm^2\,min^1~\mu m^{-2}~s^{-1}})$ ; A is the surface area (in cm²) of the sample exposed to solution;  $\nu$  is surface

retreat rate (in nm s<sup>-1</sup>) as the change in surface height over time ( $\Delta h/\Delta t$ );  $V_m$  is the material molar volume, which is  $1.0 \times 10^{-5}$  m<sup>3</sup> mol<sup>-1</sup>.

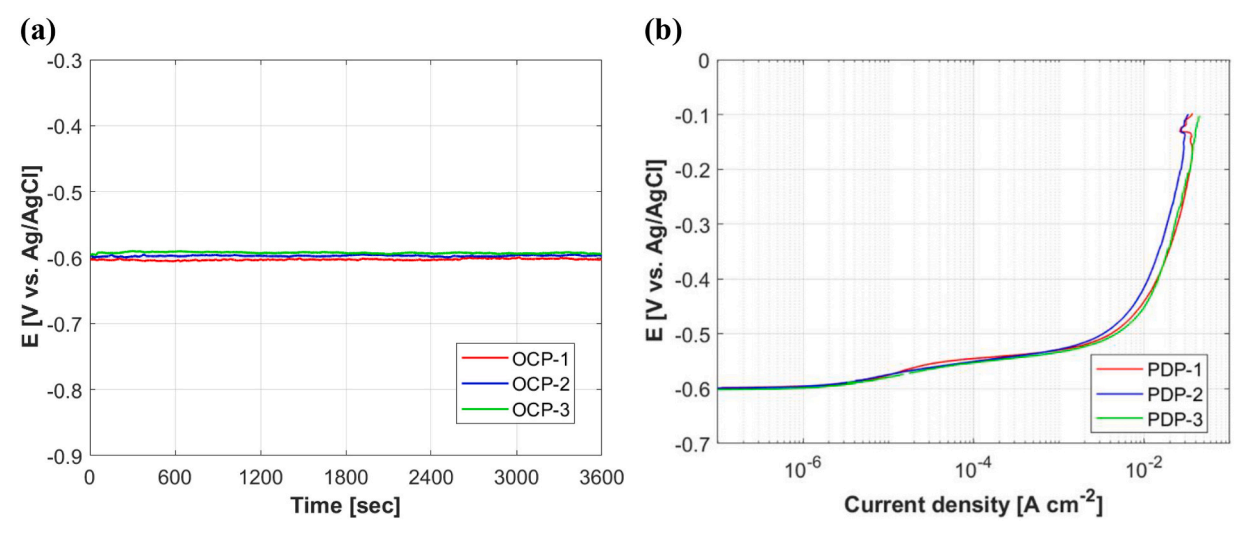
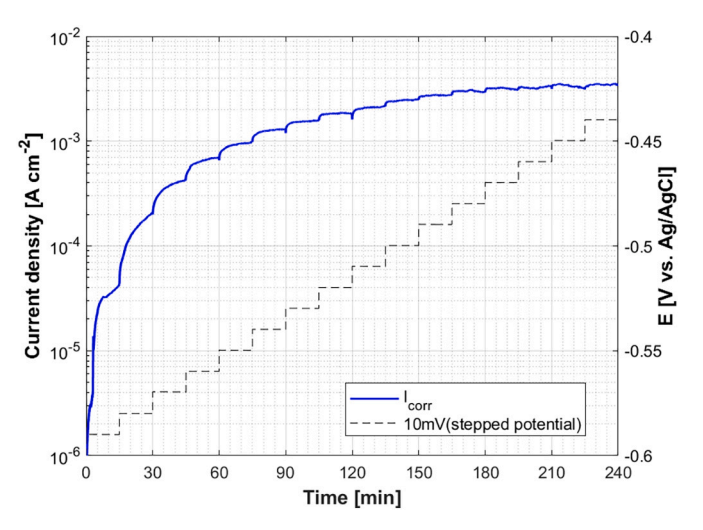


Fig. 4. (a)  $E_{oc}$  as a function of immersion time and initial concentration of acidified 0.5 wt% NaCl. (b) replicates of PDP curves for polished AA6111 in acidified 0.5 wt% NaCl.



**Fig. 5.** Current density (*i*) and potential data from stepwise polarization test showing the methodology of the applied potential and current response for the alloy samples. The potential was stepped up in 10 mV (vs. Ag/AgCl) increments at intervals of 15 min for 240 min.

#### 3. Results and discussion

#### 3.1. Electrochemical results

Electrochemical tests for AA6111 alloy in acidified 0.5 wt% NaCl solution was performed with potentiodynamic polarization (PDP) experiment.  $E_{0c}$  was first measured to determine the stability before the electrochemical test of the system. After 1 h of immersion, all bulk samples reached a stable potential of approximately -0.6 V vs. Ag/AgCl(Fig. 4a). The potential-logarithmic current density behavior at the anodic scan of +0.5 V after  $E_{oc}$  stabilization is shown in Fig. 4b. The  $E_{oc}$ and PDP results performed on the fluid cell in a flowing state showed a high level of replicability. As one may indicate, the polarization curves from the bulk samples are almost identical in shape and form with the  $E_{oc}$  starting at -0.6 V vs. Ag/AgCl. The anodic behavior is dictated by active dissolution as typified by an acute increase in i at potentials above  $E_{oc}$  [88]. Comparing each sample, an average pitting potential is noted between -0.55 V vs. Ag/AgCl, which describes an attack on the alloy surface leading to corrosion initiation. The i above the breakdown pitting potential is the limiting current density (ilim). Within this

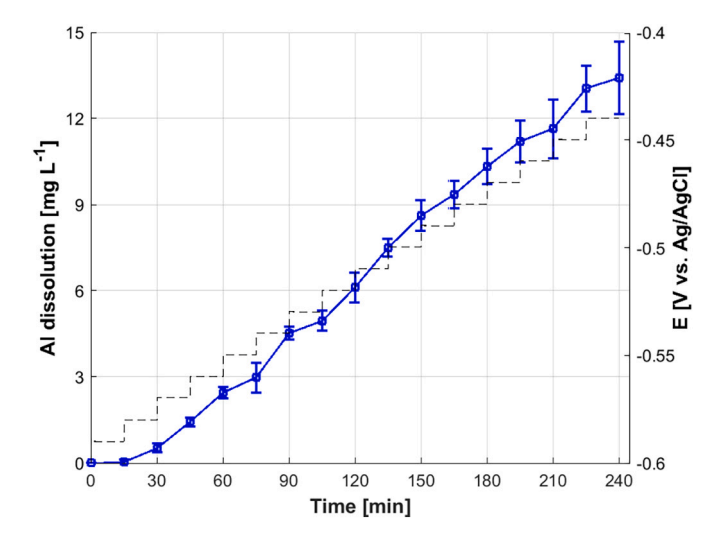


**Fig. 6.** Al concentration in the bulk solution at each applied potential with time. Note: Other secondary elements such as Mg, Cu, Si, Fe, or Mn were present in much smaller quantities or not detected in the bulk solution. The error bars represents the standard deviation.

potential range, the initiation sites for corrosion damage are either dominated by pitting corrosion and/or IGC in the matrix adjacent, which could be from secondary phases, grain boundaries, or specific phases at grain boundaries [91]. Consequently, a stepwise polarization test was therefore conducted, as was described in Section 2.2. With the potential applied in a stepwise manner, the resolution of the potential scan is increased and the quality SMI surface topography images can be captured adequately in real time. At each potentiostat step holds, I was collected as a function of time at the rate of 0.5 Hz. In total, three replicates of the stepwise potentiostatic polarization curve were measured, and the average is plotted in Fig. 5. The individual replicate curves are shown in the Supplementary Material as Appendix B.

# 3.2. Solution composition and surface characterization

Analysis of the electrolyte solutions was applied to provide elemental dissolution rate on time-dependent corrosion processes in bulk corrosion. Aliquots of outflow solution were analyzed for aluminum (<sup>27</sup>Al) per standard method 3125-B. Samples and calibration standards were

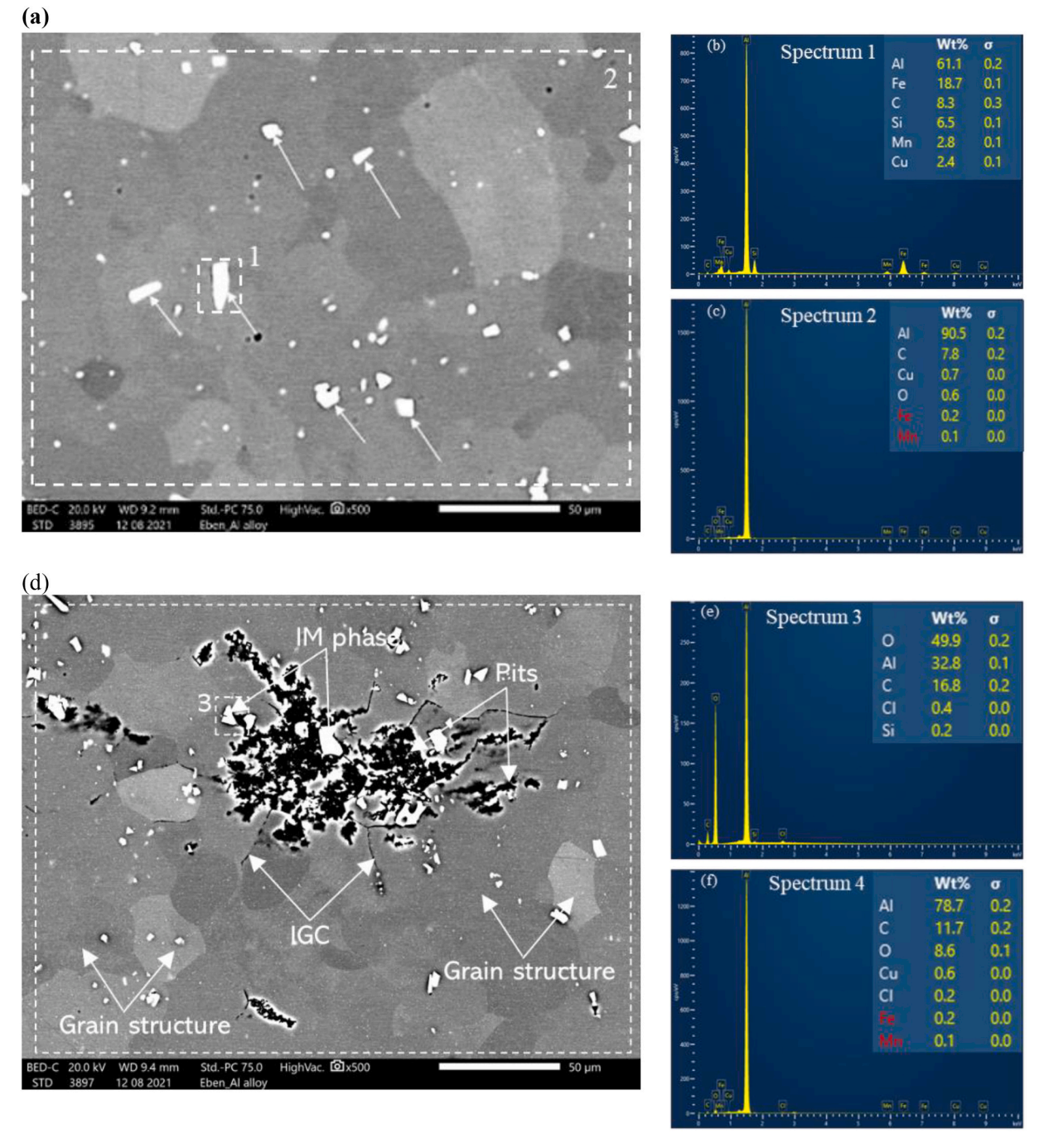


Fig. 7. (a) SEM micrograph of polished alloy surface before corrosion attack, (b) EDS analysis illustrating the chemical composition of the IM phase before corrosion (Spectrum 1), and (c) EDS analysis of the alloy matrix before corrosion (Spectrum 2). (d) SEM micrograph of the corroded sample showing both pitting and IGC corrosion, (e) EDS analysis after corrosion attack of the IM phase (Spectrum 3), and (f) EDS analysis of the bulk alloy after corrosion (Spectrum 4).

initially prepared in a matrix of 2% nitric acid by volume. The concentration of  $^{27}{\rm Al}$  was then determined in undiluted outflow solutions at each applied potential. Fig. 6 shows the ex situ time-dependent  $^{27}{\rm Al}$  concentration from the bulk solution at the beginning and end of each stepwise applied potential. The dissolved Al signal commenced from Al  $\sim$  0.04 mg L $^{-1}$  after the first step and continued to steadily rise to a maximum of  $\sim$ 13.4 mg L $^{-1}$  at the end of the experiment duration. The observed increase of Al concentration in the solution can be explained by the content rate of corrosion attack with time [92]. The significant increase in Al dissolution can be due to the instability of the oxide layer, as reported by Homazava et al. [93]. Other elements within the alloy composition were analyzed but only Al alloy is reported in this study.

Fig. 7 shows the SEM micrographs of the polished and corroded sample surface. Without surface etching, fibrous grain structures (i.e., elongated grains) are revealed across the fresh alloy (Fig. 7a). The corresponding elemental composition of the bulk surface is shown in Fig. 7b, with structures mainly made of Al. The bright features (indicated by white arrows) are the intermetallic (IM) phases that contain Al-Fe-Si-Mn-Cu compounds, as confirmed by EDX analysis in Fig. 7c. Fig. 7d shows the SEM micrographs of the alloy surface after corrosion attack after the stepwise anodic polarization. After corrosion, the attached grain boundaries appear as dark bands, suggesting both pitting and localized IGC corrosion of the alloy. The pitting corrosion initiation of Al alloys is induced by the stability of the oxide layers and the

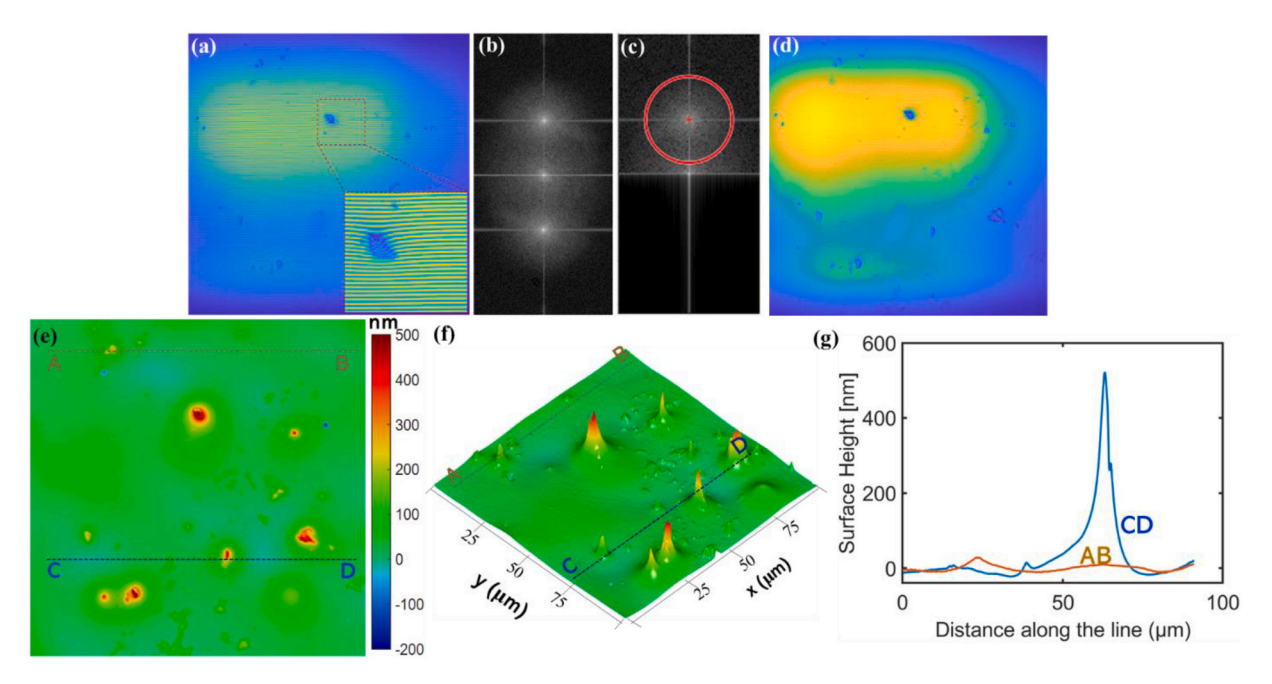


Fig. 8. The phase demodulation procedure of SMI-based quantitative phase imaging on the alloy sample: (a) 2D interferogram (as described by Eq. 4) with the inset of a magnified view of the local interference; (b) 2D zero-padded FFT of the interpolated interferogram; (c) Hilbert transform of (a) with the highlighted circle indicating bandpass filtered signal; (d) the demodulated brightfield image of the sample (e) height map of the sample (100  $\mu$ m  $\times$  100  $\mu$ m FOV); (f) 3D rendered height map of the sample; (g) the cross-sectional height profiles along the lines AB and CD at marked positions in the 3D image. The color bar indicates the change in surface topography (in nm) for Figs. 8e and f.

presence of the IM particles, acting either cathodically or anodically relative to the alloy matrix [94,95]. Hence, Al concentration in the solution occurs in the oxidized form, and the Al<sup>3+</sup> is released from the bulk matrix and the IM phase. As confirmed by the EDS result (Fig. 7b and e), alloy matrix is corroded as shown in percent Al loss.

#### 3.3. SMI results

The reconstruction of surface height images from SMI interferograms is illustrated in Fig. 8. The 2D interferograms are formed from the interference of light on the spectrometer between the sample and reference beams (Fig. 8a). A zero-padded 2D fast Fourier transform (FFT) is performed on the interferogram, revealing the modulated and baseband signals described by Eq. (4) (Fig. 8b). The positive frequency bandpass signal, containing the sample phase information, is isolated via multiplication in the frequency domain with a raised cosine filter ( $\beta = 1$ ) with cutoff frequency defined by the red circle in Fig. 8c. Following isolation of the complex bandpass signal, the signal is shifted to baseband via multiplication with a complex exponential with frequency opposite to the bandpass carrier frequency. With the signal at baseband, the signal phase and amplitude can be extracted. The amplitude signal describes interference amplitude or the coefficient of the cosine term in Eq. (4). This image (Fig. 8d) is similar to traditional brightfield optical micrographs and represents the product of light intensity reflected from the sample and reference surfaces. The extracted phase signal is then unwrapped using the Goldstein algorithm [96]. The unwrapped phase can then be converted to optical pathlength by the appropriate wavenumber for each pixel on the spectrometer. The OPL image background is masked and fit to a 15th order Zernike polynomial, which is subtracted to remove system phase aberration of the SMI interferometer. The background-subtracted OPL is then converted to surface height by dividing by the medium refractive index (i.e., n = 1.33 for water immersion imaging) and displayed in Fig. 8e.

The final surface height and brightfield images from SMI use a scanning area of 100  $\mu m \times 100~\mu m$  field-of-view (FOV) in the sample plane with 1024-pixel spectral  $\times$  512-pixel scanning. As the surface

height image represents the topography of the sample surface, it can be rendered in 3D with computed lighting to better visualize small surface features (Fig. 8f). 1D plots can of the surface height (Fig. 8g) can be produced along lines of interest to quantitatively show the heights of surface features such as background surface curvature (AB) and intermetallic phases (CD). A detailed view of the 3D image demonstrates a relatively smooth surface, with special features of grain orientations and IM phases (as expected according to the SEM micrograph in Fig. 7a).

#### 3.3.1. SMI sample height reference

The absolute height changes in SMI or other holographic measurement requires a flat-surface reference plane that remains at constant elevation during the entire experiment. Application of reference masks, such as deposition of thin film of chromium or gold, is often used for mineral surface studies [64-66]. However, the use of such conductive masks that are noble to Al would add a galvanic reaction and affect the measurement of electrochemical behavior and dissolution kinetics of alloy materials [69]. Thus, the use of a reference mask was avoided in this study. Because the spatial distribution of rate contributors is not homogeneous (as seen in Fig. 9a), investigating a flat subregion with no pit formation could bring insight to the dissolution mechanism in the sample. For this purpose, a selected subregion of 10  $\mu m$   $\times$  10  $\mu m$ (squared in red in Fig. 9a) within the FOV was analyzed throughout the experiment and also serve as the reference height from which the relative surface height change is measured at the specific region of interest (ROI). The analysis of the chosen subregion is based on the selection of corroded images at the end of the experiment. The selected area was then measured by back-tracking to the start of the experiment. Fig. 9b shows the surface topography changes and its histograms after 0, 60, 120, 180, and 240 min of the selected area. The complete surface topography map at 15 min interval corresponding to the stepwise potential applied (Fig. 5) and cross-sectional mp4 video plot of pit evolution with the background surface remain unchanged are available for download in Appendix C of Supplementary Material. The average dissolution rate of the subregion is observed to be approximately constant during the entire experiment with a comparable mean surface

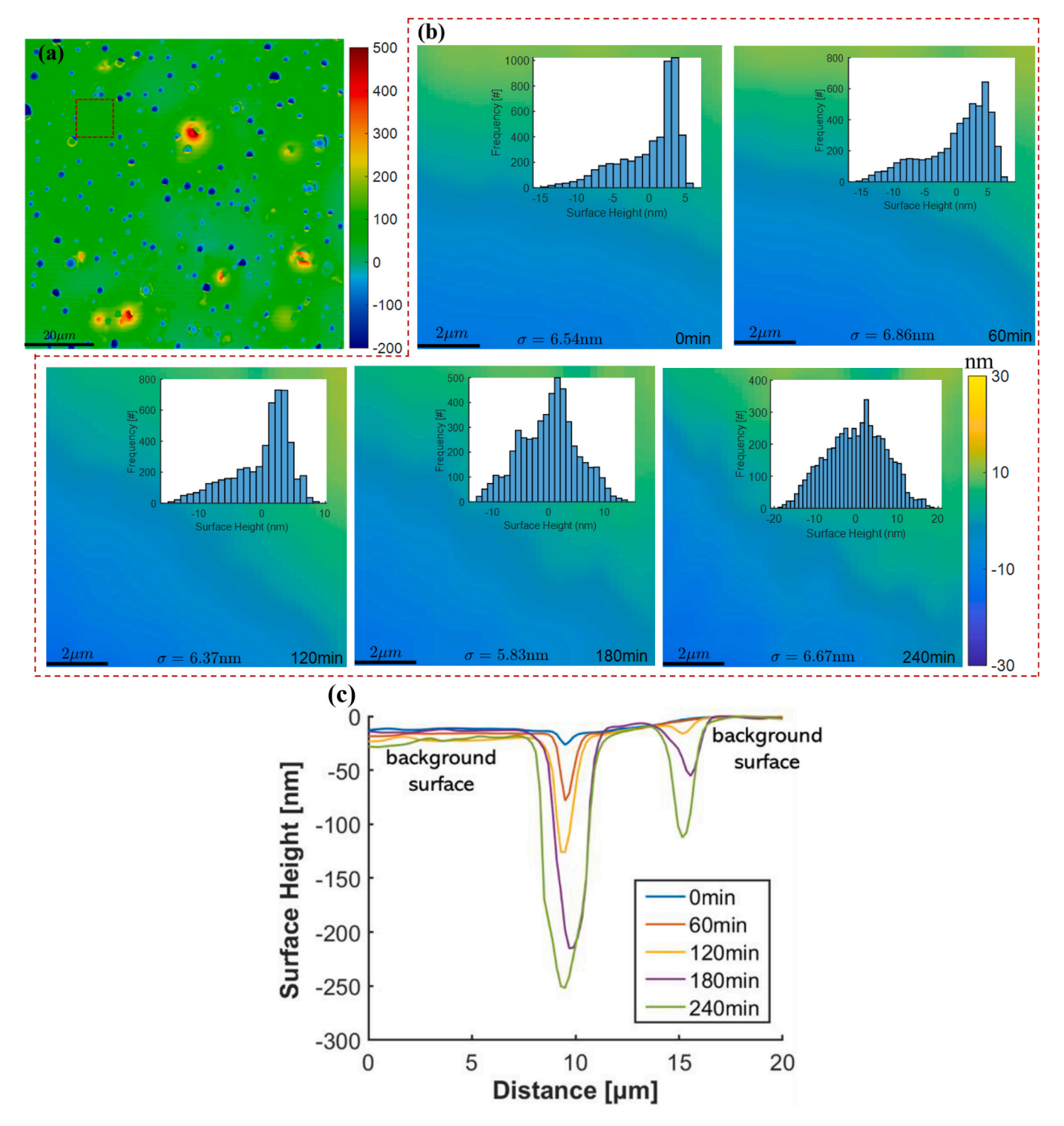
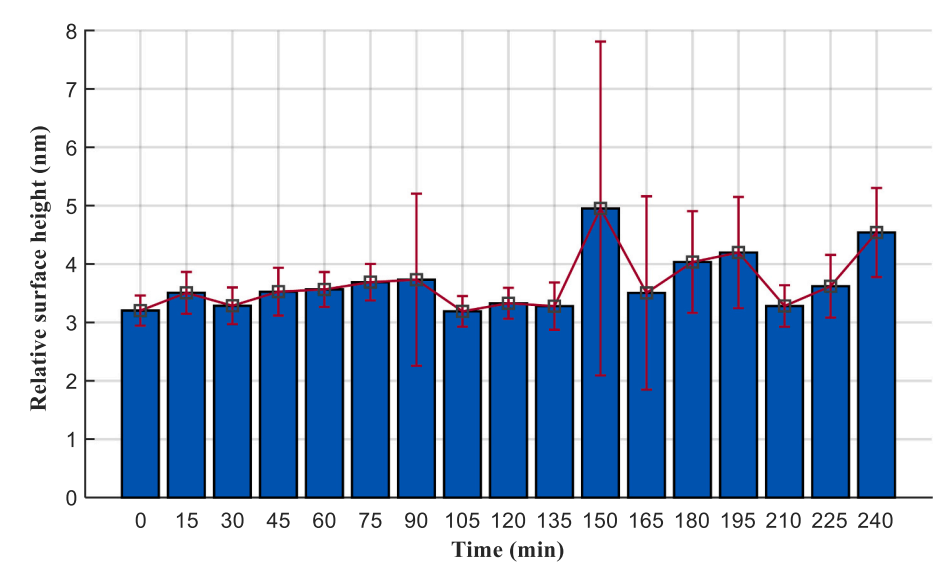


Fig. 9. (a) Final SMI height map at the end of the experiment, illustrating non-homogenous dissolution across the surface, with the image showing the selected flat subregion (squared in red) for the analysis. (b) SMI surface topography map of  $10~\mu m \times 10~\mu m$  flat subregion at 0 min, 60 min, 120 min, 180 min, and 240 min. The baseline height at the ROI surface remains approximately constant with time, which indicates no dissolution. The color bar indicates the change in surface topography (in nm). (c) cross-sectional plot of pit evolution (pit grows deeper) with the background surface remain unchanged. (For interpretation of the references to colour in this figure legend, the reader is referred to the web version of this article.)

height of 3.14 nm, 3.88 nm, 3.47 nm, 3.82 nm, and 5.32 nm at 0 min, 60 min, 120 min, 180 min, and 240 min respectively. As confirmed from the cross-sectional plot in Fig. 9c, wherein the background surface remains unchanged as pit formation evolved over the entire experiment period. It is very convincing to observe a constant in background surface region while the pits get deeper. The surface map at 240 min is somewhat high

(mean surface height = 5.37 nm), which could be due to difference in the subtracted system phase background, cloudiness (as a result of corrosion product) of the solution leading to the change in refractive index of the solution, phase unwrapping error and turbulence in the flow field, therefore, causing noisy data at the end of experiment [66,84].

Fig. 10 shows the average surface roughness profile of the flat



**Fig. 10.** Average relative surface height vs time plot corresponding to the selected flat area. The mean and the standard error were computed for every collected SMI data at 15 min interval (conforming to the stepwise potential applied) was analyzed. Based on the ANOVA and Tukey HSD analysis, the surface map of the selected area is not statistically different for every applied potential.

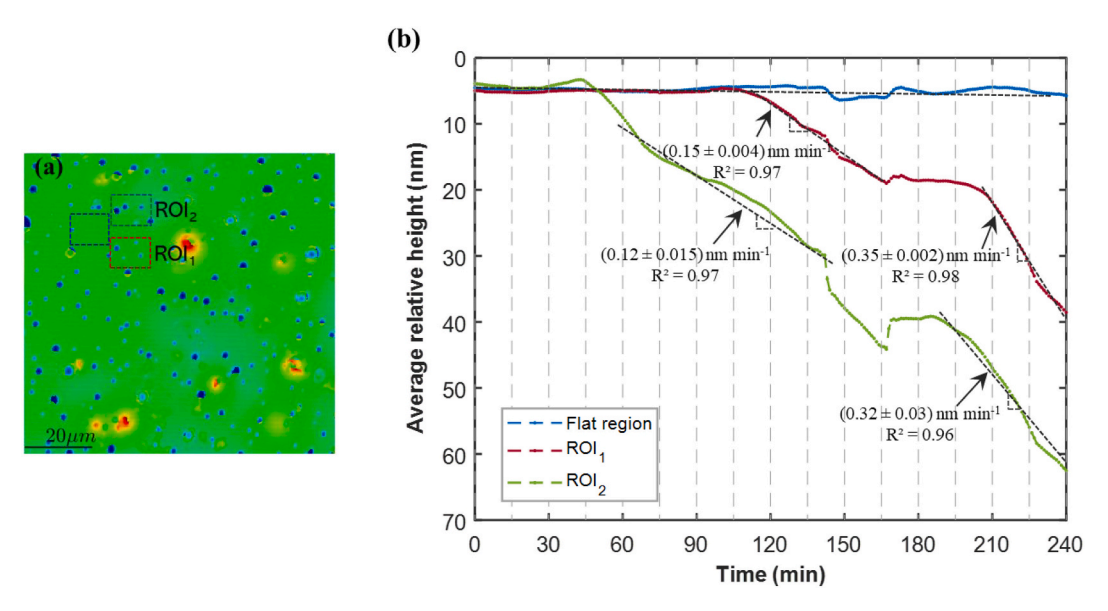


Fig. 11. (a) Surface topography map at the end of the experiment; with image showing the selected pitting subregions (squared in red and green), relative to the flat area (squared in blue) considered for the analysis. (b) The plot of average surface height from which time-dependent surface normal dissolution velocities are computed (i.e., calculating the slope of the linear regression of the height data over the selected interval). Uncertainties reported for each slope measurement are the standard errors of regression. The dip in ROI<sub>2</sub> curve from 130 to 170 min could be due to the phase algorithm as mentioned earlier in Section 3.3.1. (For interpretation of the references to colour in this figure legend, the reader is referred to the web version of this article.)

subregion at every 15 min interval. This was analyzed by calculating the mean and standard deviation of all collected surface height data at 15 min intervals, corresponding to the potential applied in the 15 min stepwise manner. The minimum and maximum relative surface height were  $[3.19\pm0.26]$  nm to  $[4.95\pm2.86]$  nm, respectively. With this small nanometer difference in surface height, no detection of uniform corrosion of alloy was observed in this selected region. Similar to the topography map, a slight increase in standard deviation was sighted at 150 min and 240 min due to errors mentioned earlier [84]. Analysis of variance (ANOVA) and Tukey honest significant difference (HSD) at 95% confidence level was performed and showed that the surface height at every interval was not statistically different, except the height profile at 150 min and 240 min. This behavior indicated smooth, non-uniform corrosion and confirmed that the generic dissolution rates are far-from-

equilibrium conditions (e.g., similar to dissolution kinetics of mineral surfaces [52,63–66]). The Gaussian distribution was also evaluated to propagate the error by sampling the surface height change based on the mean and standard error over the 15 min interval. The propagated error from the flat region is less than 4%, confirming the assertion of the smooth subregion. In addition, the frequency distribution of surface topography change at different times of the flat subregion area is available in Appendix D of the Supplementary Material. The peak height values are in the range of 2.5 nm to 5 nm, similar to the average relative height profile in Fig. 10. The peak of the distribution is somewhat lower at times greater than 150 min, caused by phase unwrapping error at those times as mentioned earlier in Section 3.3.1.

Likewise, relative to the flat subregion, two 10  $\mu$ m  $\times$  10  $\mu$ m subregions with pit formation, referred to as ROIs in Fig. 11a, were selected

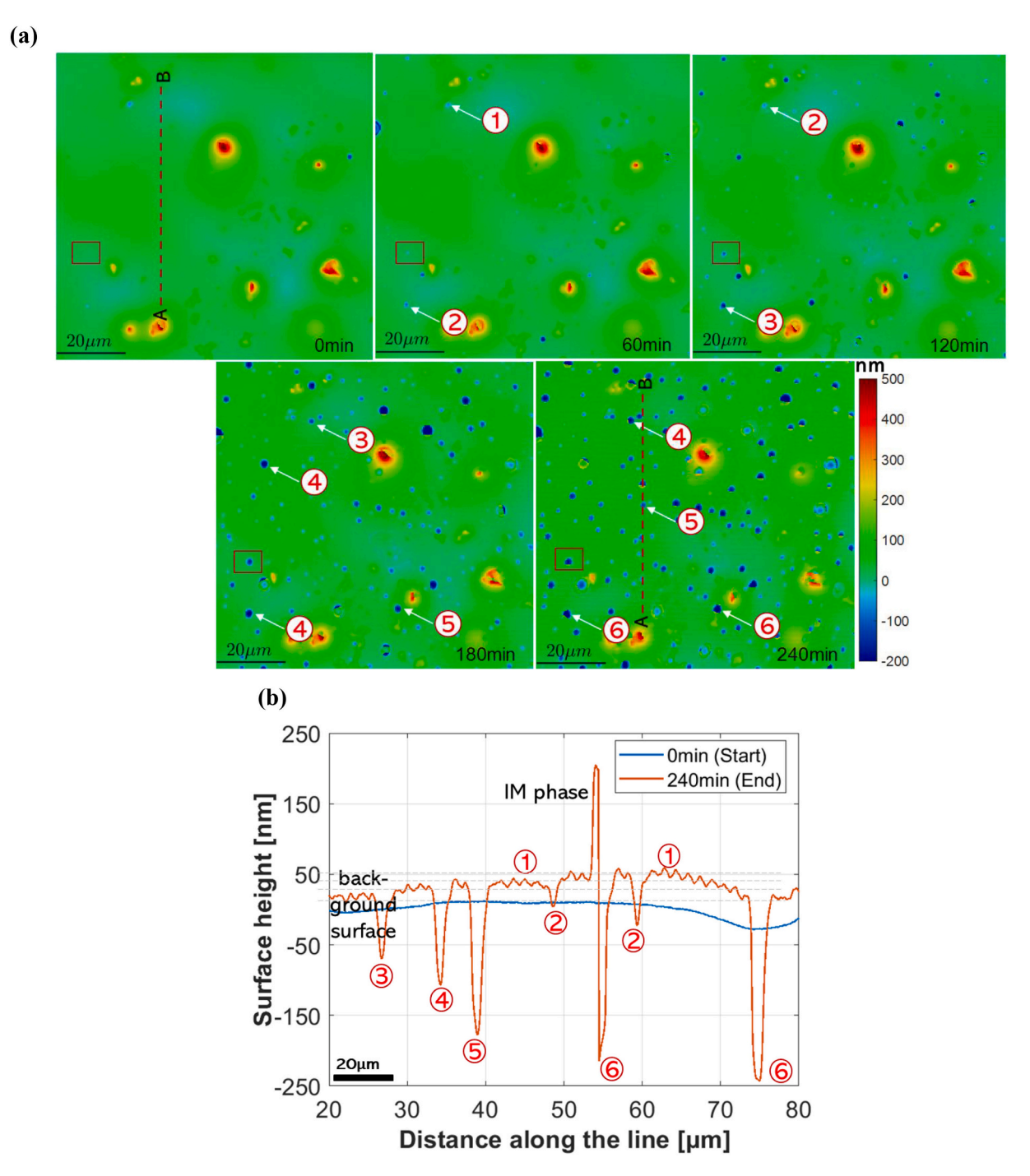
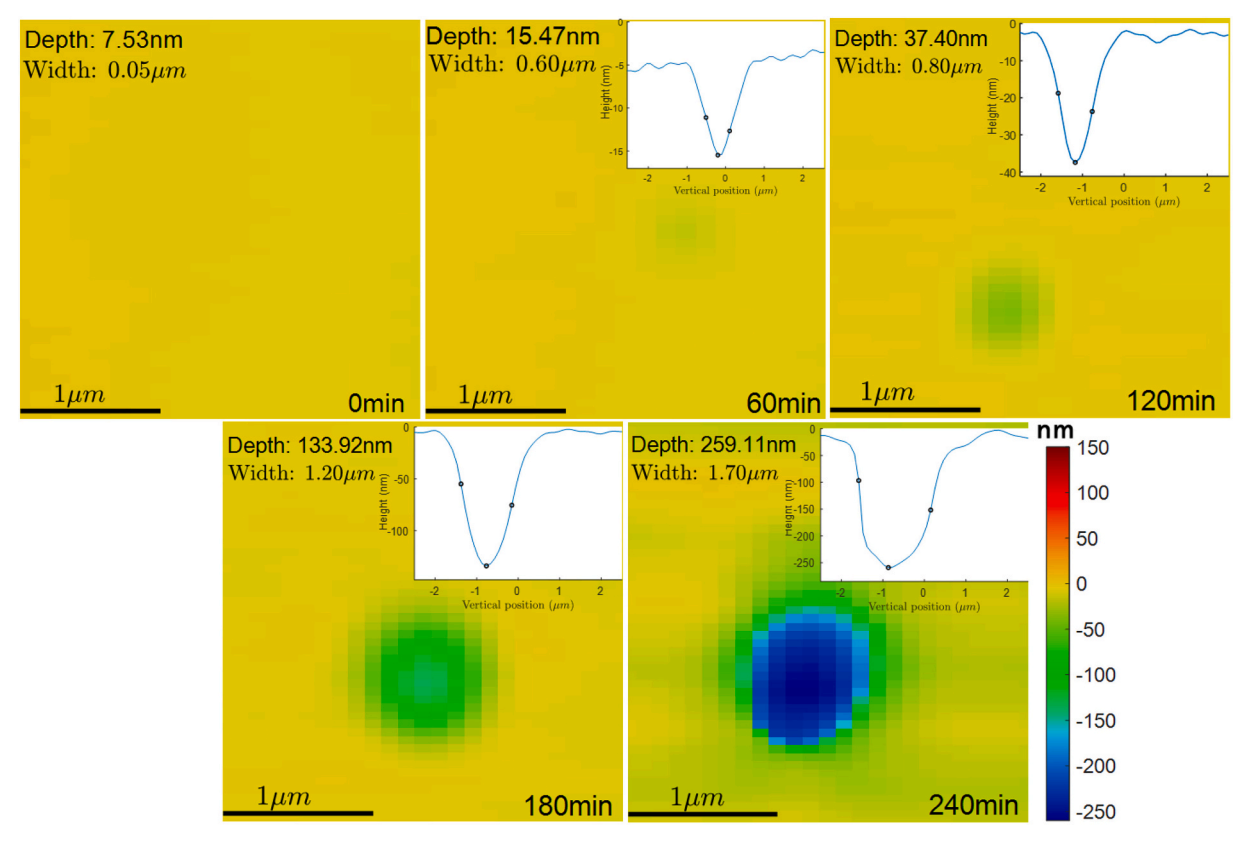


Fig. 12. SMI surface topography map of alloy sample after corrosion period of 240 min. (a) Surface map sequence for all FOV, showing frequency variation and distribution of surface pits at 0, 60, 120, 180, and 240 min. The red circle plot (1-6) illustrates height variation and red rectangle indicates a view of a specific pit over time (reported in Fig. 13). (b) Height profile plot of important surface pits variation at the end of the experiment (240 min), ranging at different level such as: [1], unreactive flat plateaus; [2], shallow pits, depth = 0 nm to 50 nm; [3], small pits, depth = 50 nm to 100 nm; [4], intermediate pits, depth = 100 nm to 150 nm; [5], deep pits, depth = 150 nm to 200 nm; and [6], very deep pits, depth > 200 nm. (For interpretation of the references to colour in this figure legend, the reader is referred to the web version of this article.)

and analyzed. Fig. 11b demonstrates the average surface height change of the flat and pitting subregions considered over the experiment period. For ROI $_1$  and ROI $_2$ , linear regression was performed on the discrete height vs. time data within different time intervals and the slope was taken as the mean normal dissolution velocity for that interval. This was assessed to account for the possible dissolution rate observed from this time-dependent height profile plot. As shown in Fig. 11b, a constant height profile with no dissolution rate of the flat 10  $\mu m \times 10~\mu m$  subregion is observed. While the average height profiles and time-

dependent surface normal dissolution velocities (based on the slope of the linear regression) of both  $ROI_1$  and  $ROI_2$  increase with time. While their pits nucleation of the two regions might be out of shift, however, their slopes, transition and propagation follow a similar trend. For instance, the pits in  $ROI_1$  initiated after 105 min, corresponding to the 6th step of the applied potential of -0.54 V vs. Ag/AgCl, whereas pits in  $ROI_2$  started earlier after 45 min at the 3rd step of the applied potential of -0.57 V vs. Ag/AgCl. Also, the distribution of pits reflects sometimes linear (*i.e.*, corresponding to an approximately constant surface normal



**Fig. 13.** SMI snapshot of a randomly selected pit (indicated with a red rectangle in Fig. 12), representing a typical pit evolution at 0 min, 60 min, 120 min, 180 min, and 240 min. Images reveal the evolution of both lateral (width) and vertical (depth) dimensions of the pit obtained during the corrosion period. Color bar height range = 400 nm. (For interpretation of the references to colour in this figure legend, the reader is referred to the web version of this article.)

velocity) and sometimes nonlinear dissolution, as shown in Fig. 11b. The possible nonlinearity observed for the time-dependent height shows that the dissolution rate is not homogenous over time, which could be due to the multiple pits in the same region, as each initiated at a different time and thus may have different rates.

# 3.3.2. Corrosion morphology and pit analysis

SMI measurements provide surface topography data and thus inform about the evolution of the corrosion process. Fig. 12 shows the surface topography evolution of  $100~\mu m \times 100~\mu m$  FOV obtained during the corrosion of the alloy sample during stepwise potentiostatic measurement. The topography features on the surface contain several pits with various sizes and shapes (i.e., smooth and flat regions without evident defects, shallow pits, and deep pits). At the start of the experiment, no formation of pits was initially observed, with the first set of pits forming within 30 and 60 min (i.e., between the 3rd and 5th step of applied potential), as seen in Fig. 12a. Other pit sites nucleate at different times and locations as the experiment proceeds. This is also confirmed in the illustrated cross-section height profile and the 3D surface plot in Fig. 12b, with variations in pit depth at the end of the experiment.

In general, pits were classified in 6 "types" from the data shown in Fig. 12: Pit type 1, unreactive flat plateaus; Pit type 2, shallow pits, depth = 0 nm to 50 nm; Pit type 3, small pits, depth = 50 nm to 100 nm; Pit type 4, intermediate pits, depth = 100 nm to 150 nm; Pit type 5, deep pits, depth = 150 nm to 200 nm; and Pit type 6, very deep pits, depth > 200 nm. This variability in depths ranges from 25 nm to approximately 250 nm, revealing the level of diversity in pit formation. Toward the end of the experiment, the alloy surface then became rougher and the topographical features continues to grow significantly. For a detailed comparison, surface topography evolution images at 15 min intervals, including a 3D video (mp4) of pit evolution and growth with time are presented as Appendix E of the Supplementary Material. Thus, this

height profile visualizes and quantifies the heterogeneous dissolution nature of the sample resulting from the applied potential.

For better visualization of pits' nucleation and growth, an additional snapshot of a randomly selected pit is also presented. Fig. 13 represents an example of the 2D reconstruction of a pit forming, disclosing the evolution of both lateral and vertical dimensions obtained during corrosion attack. The evolution of pit size and depth became noticeable after 120 min and increase accordingly over the reaction periods. By cross-sectioning the topography image, the amount variation of pit width (in  $\mu m$ ) and depth (in nm) in that region can be obtained over time. Pit depth was calculated for each region by taking the difference between the highest surface height in the region (flat background) and the deepest part of the pit. Pit width was calculated by analyzing pit cross-sections through the deepest part of the pit at each time point. For each pit, a discrete spatial derivative was applied along the cross-section to yield a global minimum and maximum corresponding to the left (falling) and right (rising) edge of the pit. The difference in position between the right and left edge yield the width of the pit. This shows both pit time of nucleation and the corresponding propagation over the entire experiment. Interestingly, the pit nucleated immediately after the applied potential is being stepped up (i.e. at the start of the ninth step). Moreover, the vertical growth rate is slightly greater than the lateral growth rate over the experiment period. For instance, the pit was primarily detected at depth and width of 37 nm and 0.8 µm, respectively, and, after 240 min of corrosion reaction, the pit depth has increased to 260 nm, which equals seven times the initial pit depth while the lateral size doubled to  $1.7 \mu m$ . In this regard, the SMI data visualize the spatial occurrence of these pits. The SMI surface map also shows (Fig. 13) the typical characteristic shape and size of a pit with higher lateral and vertical resolution. Therefore, SMI was able to provide quantitative information that explain such remarkable pit formation of an alloy sample, due to its high spatial and temporal resolution capability.

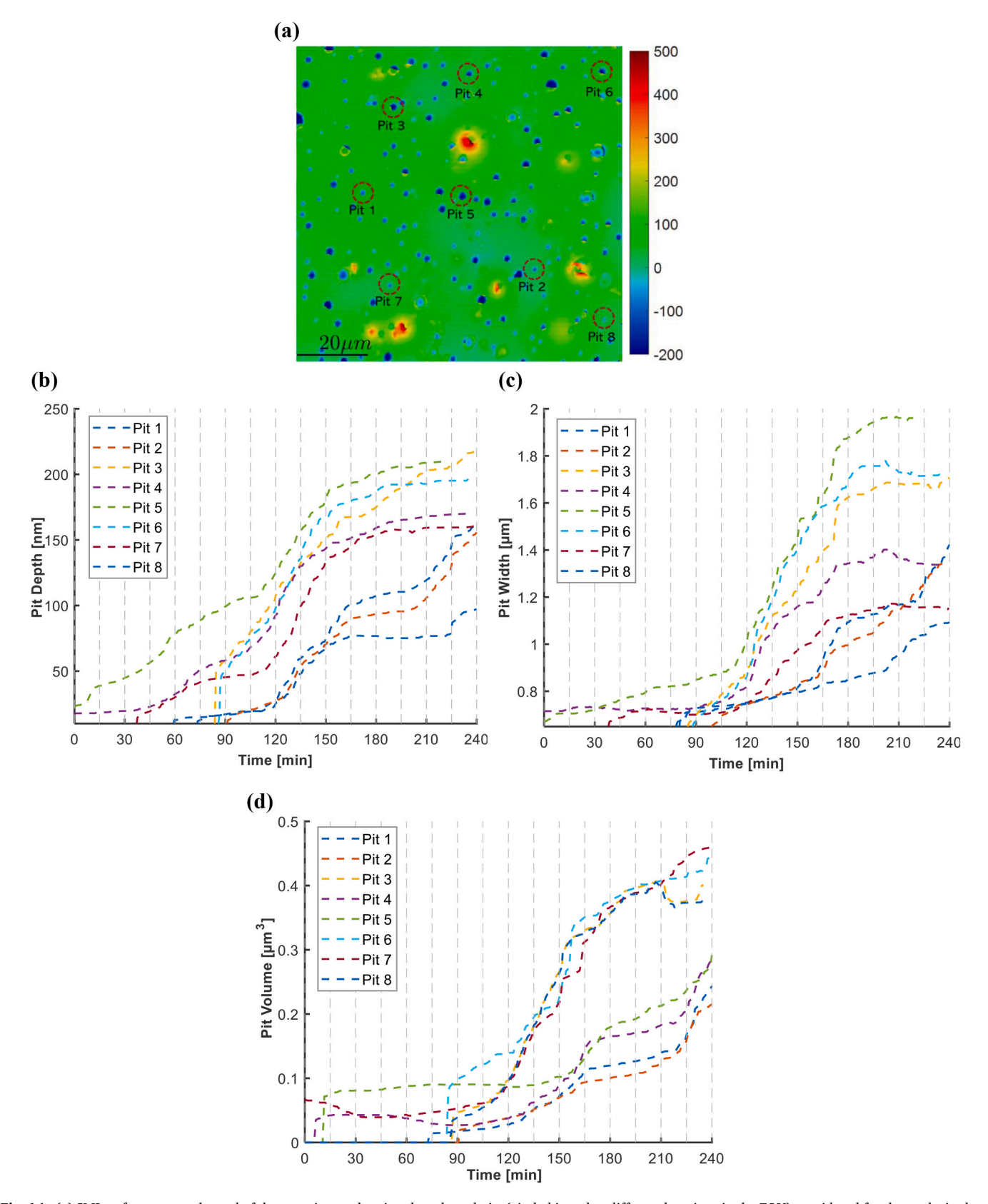


Fig. 14. (a) SMI surface map at the end of the experiment showing the selected pits (circled in red at different locations in the FOV) considered for the analysis along with the time-dependent pit (b) depth, (c) width, and (d) volume. Pit parameters were analyzed from the acquired *real time* SMI data of 240 min with a total of 480 images. The color bar in 14a indicates a height range of 700 nm. (For interpretation of the references to colour in this figure legend, the reader is referred to the web version of this article.)

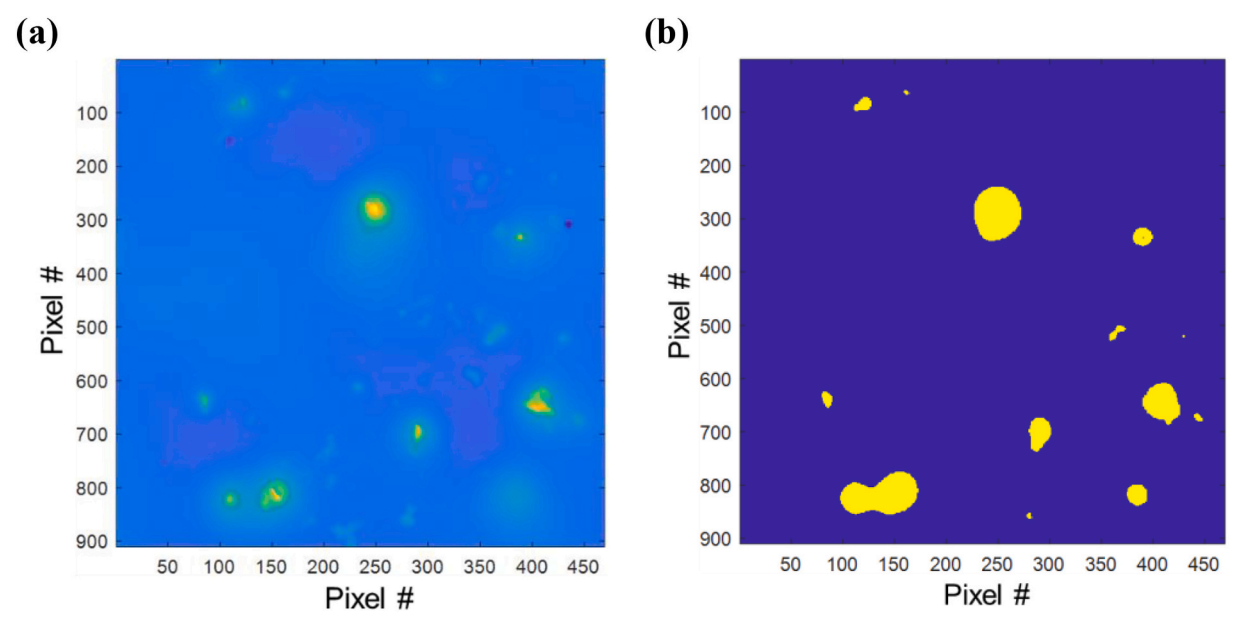


Fig. 15. (a) SMI topography map at the start of the experiment and (b) profile of created mask on the sample FOV during post-processed, with IM phases removed from the image (10pixel is 1 μm).

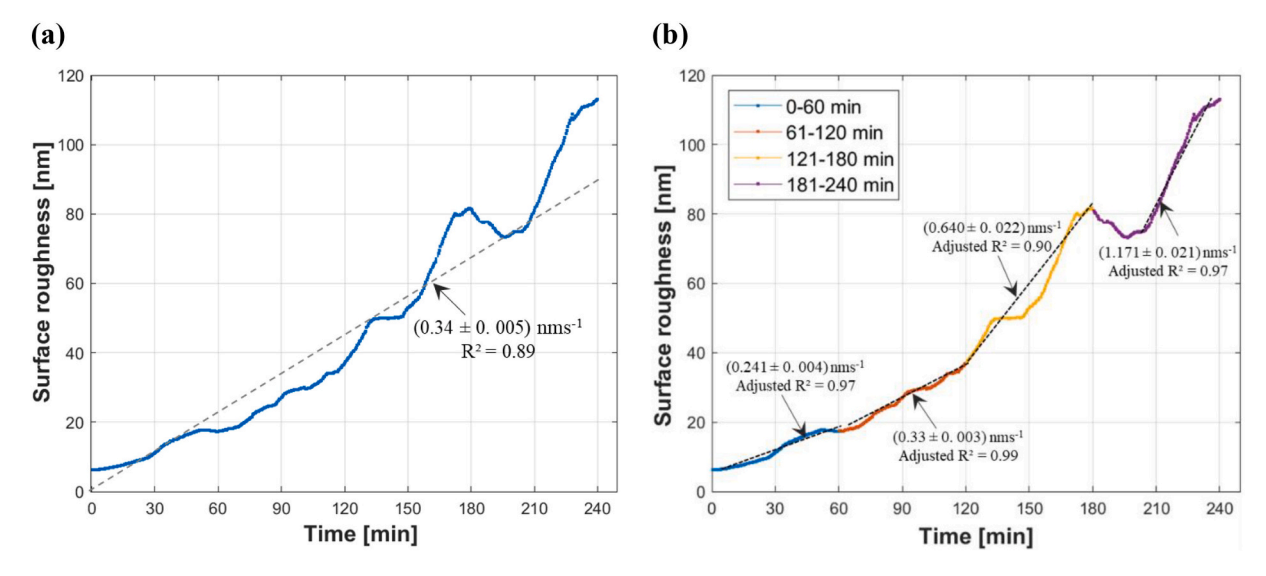


Fig. 16. Time dependence of surface roughness within entire FOV during corrosion experiment. Dissolution fluxes are estimated by linear regression, and each reported uncertainty is the standard error of regression for the associated line segment. (a) Example of time-dependent surface normal dissolution velocities computed for the entire corrosion period; (b) Example of the time-dependent surface normal dissolution velocities computed at 60-min interval corrosion period.

Fig. 14 presents in situ time-dependence of pit parameters (i.e., pit width, pit depth, and derived pit volume) of 8 pits at different locations across the FOV. The analysis of these pits comprises different pit sizes, ranging from small to very deep, that majorly contribute to the overall dissolution rate. Of note, these pit parameters were computed from the acquired real time SMI data during the entire experiment, and images with phase unwrapping error were neglected in the analysis. As shown in Fig. 14a, the pit depth generally increases over time, with different morphologies of pit evolution with time. The variability of pit depth ranges between 90 nm and 230 nm, with nucleation occurring at a different time of corrosion period. For instance, Pits 4 and 5 are initiated at the start of the experiment, while Pits 1, 3, and 6 form after 90 min of the corrosion period has been completed, confirming the temporal heterogeneity in dissolution of the alloy sample. Likewise, pit growth across different locations is not always uniform or symmetrical. For example, the pattern of formation for Pits 1 and 3 is more diverse, even

though they nucleated within a similar period, whereas the growth of Pits 3 and 6 follow similar prototypes over the experiment period. Therefore, the capability to accurately predict the initiation of pits in real time and its propagation pattern over the corrosion period makes SMI a new technique for nanoscale quantitative evaluation of corrosion. Again, the formation and growth pattern of pits width is identical with pit depth and within range (1 to  $2 \mu m$ ) after the experiment (Fig. 14b). This is a new finding compared to the previous corrosion study that reported an almost constant pit formation [10]. Likewise, the data for the variation in pit volume, as a function of time is presented in Fig. 14c, following the trend observed in the formation of lateral and vertical pits. Pit volume was calculated by a discrete 2D summation of all surface heights within the pit. The pitting nucleation and propagation analysis during the experiment were based on the collection of growing pits from the final SMI image and then measured by tracing back through the formation (growth) of the selected pits until they disappeared.

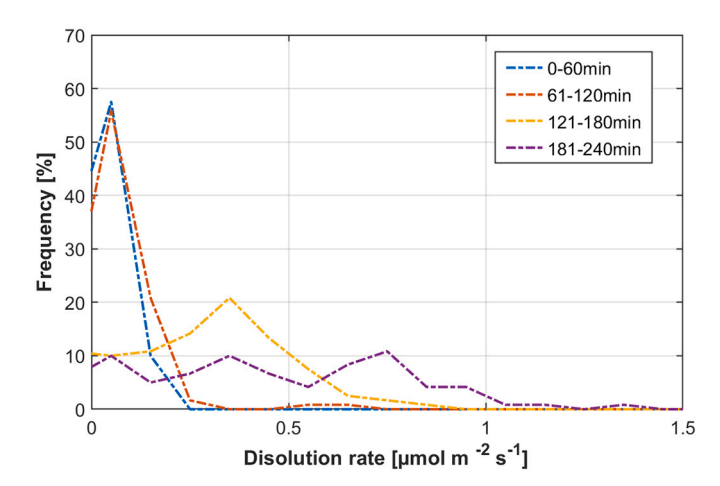


Fig. 17. Surface normal dissolution rate spectra at 60-min intervals of the entire FOV from experiments conducted.

#### 3.3.3. Surface topography analysis and dissolution rates

The *in situ* SMI time-series of surface data collected can be used to quantify and visualize the surface topography evolution, material dissolution flux, and the frequency of rates that contributes to the overall surface corrosion. Of note, the surface roughness parameters such as root-mean-square (RMS) roughness as seen in Eq. (5), where N is the number of unmasked pixels used for the RMS calculation, and h(j) is the sample surface height at each pixel, have been previously used to produce this quantitative information [52,97].

$$RRMS = \sqrt{\frac{1}{N} \sum_{j=1}^{N} [h(j)]^{2}}$$
 (5)

Thus, the RMS parameter was then calculated for the entire FOV of size  $100~\mu m \times 100~\mu m$ , excluding regions with IM phases, using the 480 total images. With this roughness parameter, the heterogeneous contribution to the overall surface that is, the occurrence and

distributions of building blocks of pits across the surface can be computed quantitatively. To avoid the impact of surface IM phases (*i.e.*, micro features as in Fig. 8e) on the analysis of surface dissolution rate, a mask was generated via a global surface height threshold on the entire FOV to digitally remove those phases during post-processing, as seen as the yellow regions in Fig. 15b.

The time dependence of RMS for all data point FOV during the corrosion period of 240 min is shown in Fig. 16. As expected, the surface height increases with increasing corrosion activity. The initial height value was <10 nm, which indicates a very flat surface. After the corrosion steps, a rougher surface and significant pits growth were observed with a higher height value (e.g., RMS > 100 nm). Compared with the electrochemical data, the low RMS value at the initial reacted surface (correspond to a less applied potential mV) is caused by the limited number of such pits prior to a longer dissolution period (when higher potentials have been applied). Notably, the plot of RMS versus time is sometimes approximately linear and sometimes is nonlinear (Fig. 16a). For instance, the roughness parameter during some reaction steps was approximately constant, as was obvious at time steps from 135 min to 150 min and from 180 min to 210 min, this behavior indicates that dissolution rates are more characterized as a heterogeneous distribution than single linear relation [52,54,62]. Though a slight descending roughness value was noticed between 180 min and 210 min, this may be due to noisy data (as reported earlier in Section 3.3.1). Similarly, the obtained pits' formation (i.e., the pits' width, depth, and volume in Fig. 14) converged with the RMS value for the entire FOV; thus, the topography distribution features ranging from shallow pits (Pit 1) to very deep pit depths (Pit 6) are also in effect across the entire surface.

Afterward, dissolution fluxes of the entire FOV were estimated from the *in situ* quantitative height profile at a nanoscale via linear regression. Linear regression across all observations (*i.e.*, from 0 to 240 min) was first taken (Fig. 16a); however, this does not produce an accurate representation of the data because of the heterogeneity of the sample's corrosion rate and does not account for the possible nonlinearity observed for the time-dependent height measurements. For this reason, a linear regression over 1-h intervals (Fig. 16b) was used to compute the

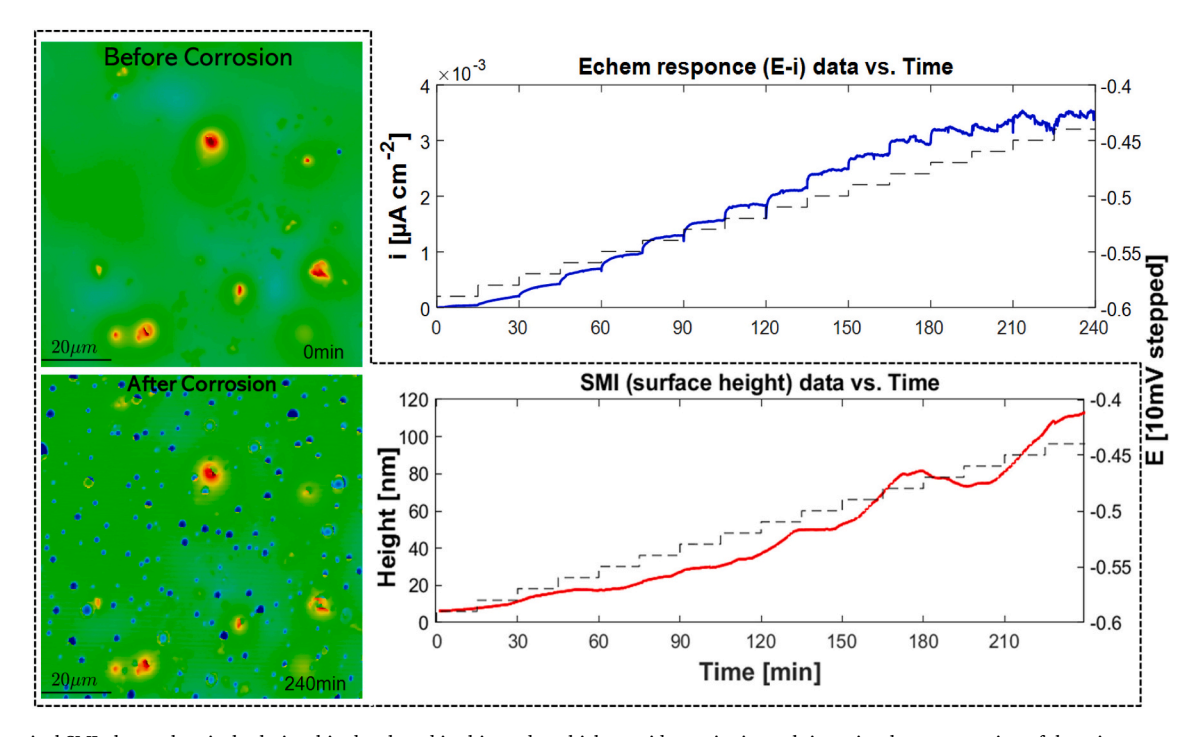


**Fig. 18.** A typical SMI-electrochemical relationship developed in this study, which provides an *in situ* real time visual representation of the microstructural corrosion modes and the surface topography change with time, as well as potential, (E)–current response, (i).

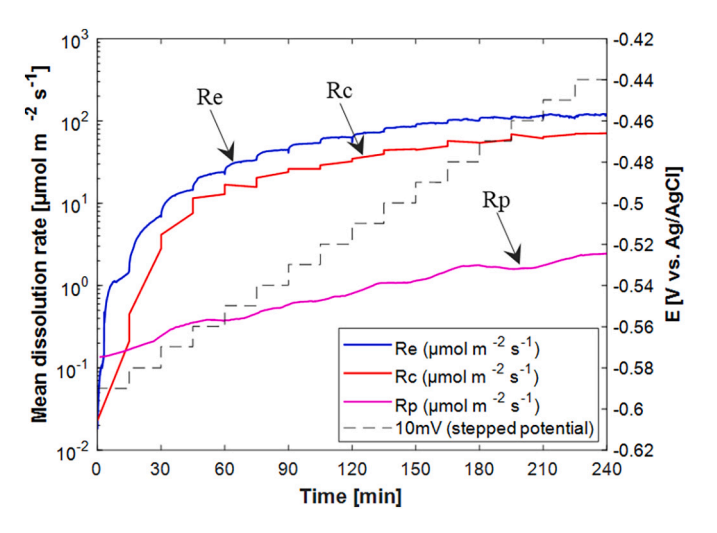


Fig. 19. Three collaborative measurements of dissolution rate kinetics were computed from an electrochemical test, solution composition analysis and nanoscale surface topography measurement by SMI. Note: analysis of the solution composition is only based on the aliquots collected at the beginning and end of each stepwise applied potential.

Table 2 Corrosion rate calculations from three assessment types (in  $\mu$ mol m<sup>-2</sup> s<sup>-1</sup>).

Measurement type	Rate equation	Equation number
Electrochemical measurement	$R_{\rm e} = K_{\rm e} (i {\rm M}/n {\rm F} \rho)/V_{\rm m}$	Eq. (1)
Solution composition analysis	$R_c = K_c f(C_i - C_o) / \eta A$	Eq. (2)
Physical surface change by SMI	$R_p = v/V_m = (\Delta h/\Delta t)/V_m$	Eq. (3)

time-dependent bulk surface normal velocity and the corrosion rate is then computed using Eq. (3). The standard errors characterizing the uncertainty of the line segment regression are also reported. First, the sample surface experienced an early period of approximately linear surface retreat, with molar fluxes inferred from linear regression of the first 60 min period of [0.40  $\pm$  0.007]  $\mu mol\ m^{-2}\ s^{-1}.$  From the 60 min to 120 min corrosion period, a faster linear dissolution rate of [0.55  $\pm$ 0.007]  $\mu$ mol m<sup>-2</sup> s<sup>-1</sup> was observed but similar in distribution to the first 60 min period. After the linear period, the rapid surface retreat began with the combination of linear and nonlinear distribution fluxes, corresponding to the 3rd hour corrosion period (120 min to 180 min). This accelerated period happens due to pit formation of different sizes as shown in the image captured in Fig. 12. The rate measured during this accelerated dissolution, obtained by linear regression is  $[1.07 \pm 0.037]$  $\mu$ mol m<sup>-2</sup> s<sup>-1</sup>, which doubled the rate of earlier steps. Neglecting the noisy data at the 180 min to 210 min interval, the new dissolution rate  $[1.95 \pm 0.035] \mu \text{mol m}^{-2} \text{ s}^{-1}$  is even faster than the previous rates, consistent with the electrochemical observation. The summary of the computed dissolution fluxes is illustrated in Table 3.

Fig. 17 shows the analyzed dissolution rate spectra obtained using the entire FOV at 60 min intervals during the experiment. The great

**Table 3**Summary of dissolution rates computed at 60 min intervals, based on the slope of the linear regression of the height data over that interval. Numbers enclosed in parentheses are the standard errors from regression.

Time interval	Slope	R <sup>2</sup> value	Dissolution rate		
(min)	$(nm min^{-1})$		$(\mu mol \ m^{-2} \ s^{-1})$		
All time points	0.442 (0.004)	0.938	0.737 (0.007)		
0 to 60	0.241 (0.004)	0.966	0.402 (0.007)		
61 to 120	0.329 (0.003)	0.988	0.550 (0.005)		
121 to 180	0.640 (0.022)	0.899	1.067 (0.037)		
181 to 240	1.171 (0.021)	0.974	1.952 (0.035)		

majority of measured rates fall between 0.05  $\mu$ mol m<sup>-2</sup> s<sup>-1</sup> and 1.5  $\mu$ mol m<sup>-2</sup> s<sup>-1</sup>. The frequency of detachment from different distinct types of surface sites, giving rise to the peaks in the distribution. At the beginning of observed period, the peak of the distribution was minimal, which corresponded to lower grand dissolution rates (as shown in Table 3) and continued to increase and reach its highest dissolution rate, as the corrosion attack continues until the end of the experiment. The mean, mode, 25th, 50th (median) and 75th percentile that correspond to the interquartile range (IQR) at 60 min intervals are also reported in Table 4. A more plateau-like frequency spectrum is noticed at the last corrosion period (181 min to 240 min), showing that at higher applied potential, a high dissolution rate with rapid pit formation occurs within the time step. Moreover, apparent negative dissolution rates were omitted from the analysis, which could be attributed to isolated errors in the unwrapping algorithm; nevertheless, the 60-min spectra rates, along with their negative rates, are provided in the Supplementary Material as

In the conventional potential–current (E–i) response, this electrochemical relationship is not adequate to model localized corrosion of passivating materials like aluminum alloys. Thus, the combination of SMI with the E–i response is valuable in providing additional data for both electrochemical and topographical changes. For example, Fig. 18 compares the time-dependent SMI and E–i data, which provide an *in situ* real time visual representation of the microstructural corrosion modes and the surface topography change with time. This will provide a direct comparison of the influence of thermal history on aluminum alloy corrosion modes and help to construct better corrosion models for practical implications and applications in corrosion engineering.

Finally, the in-situ nanoscale surface topography evolution in real time acquired by SMI is linked with the electrochemical measurement from the stepwise potentiostatic test, and outflow solution chemistry analysis of the dissolved Al. Using Eqs. (1), (2), and (3) in Table 2, the dissolution rates were evaluated from the three collaborating methods and plotted as shown in Fig. 19. Interestingly, the dissolution rates from each method follow a similar pattern during the entire corrosion period of 240 min. At the end of the corrosion period, rates of 118, 71, and 2.45  $\mu$ mol m<sup>-2</sup> s<sup>-1</sup> were obtained from electrochemical measurements, ex situ solution analyses, and in situ SMI corrosion measurement, respectively. The least rate was seen from the in situ nanoscale data acquired from SMI, which is reasonable given the small FOV of 100  $\mu m$   $\times$  100  $\mu m$ considered for the analysis. The electrochemical data gave the highest dissolution rate because the corrosion measurement is arising from the bulk sample. A slight drop in rate from solution analysis (as compared to electrochemical data) is observed, which could be due to the single element (e.g., Al) dissolution considered in the analysis. Dissolution of other elements from the bulk alloy (e.g., Cu, Mn, Mg, Fe Si) that are not being accounted for in this experiment could have led to a higher rate. In addition, it is unclear if the dissolution of this alloy in solution proceeds stoichiometrically according to its composition. Other forms of corrosion (e.g., IGC) were not seen in the analyzed 100  $\times$  100  $\mu$ m FOV, although this could have also developed somewhere, away from the FOV, and therefore was excluded from the analysis.

**Table 4**Surface normal dissolution flux statistics.

	Dissolution rate ( $\mu$ mol m <sup>-2</sup> s <sup>-1</sup> )					
Time interval (min)	Mode	Mean	Median	IQR (P <sub>25</sub> , P <sub>75</sub> ) <sup>a</sup>		
0 to 60 61 to 120 121 to 180	0.05 0.05 0.35	0.03 0.06 0.24	0.05 0.05 0.25	0.1 (0.05,0.10) 0.2 (0.15,0.15) 0.4 (0.15,0.45)		
181 to 240	0.75	0.27	0.35	0.7 (0.05,0.65)		

The 25th (P25) and 75th (P75) percentiles that correspond to the IQR.

#### 4. Conclusion

In situ nanoscale measurements have been performed in real time using novel spectral modulation interferometry (SMI) technique. Numerical reconstruction of SMI data offers real time surface topography evolution measurements with vertical resolution of a few nanometers and enables measurement of the time-dependent surface normal dissolution rates in flowing conditions. With an innovative 3D-printed fluid cell, electrochemical measurements via stepwise potentiostatic polarization test and solution chemistry through examination of collected aliquots from outflow solution were simultaneously performed alongside the nanoscale SMI data to provide three corroborating dissolution rates.

The performance of the developed fluid cell was shown from the similar polarization curves produced during the initial electrochemical test. The fluid cell configuration yields repeatable results, and the investigation of an in situ nanoscale corrosion experiment at 40 mL min<sup>-1</sup> flow condition was achievable. As shown from SMI 3D images, the topography features on the surface contain several building blocks of pits with different sizes and distributions, (i.e., smooth and flat regions without evident defects, shallow pits, and deep pits). Based on the height profile across the corroded surface, the pit sites nucleate at different times and locations as the experiment proceeds. Of noteworthy, another form of corrosion (e.g., intergranular corrosion) was not seen in the analyzed  $100 \times 100 \ \mu m$  FOV, although this could have also developed somewhere, away from the field of view (FOV), and therefore was excluded from the analysis. There is also variability in pit growth, ranging from 25 nm to 250 nm in depth and 1 µm to 2 µm in width, revealing the level of diversity in pit morphology. This describes the heterogeneous dissolution nature of the sample surface reactivity resulting from the applied potential.

Analysis of dissolution fluxes was based on the surface height change of the entire FOV. With a large FOV, the identification of heterogeneous surface reactivity caused by multiple reaction mechanisms can be readily quantified. The SMI computed time-dependent dissolution rates varied as the experiment proceeded. Initially, the sample surface due to applied potential has an early linear dissolution rate of [0.40  $\pm$  0.007]  $\mu mol~m^{-2}~s^{-1}$  and [0.55  $\pm~0.007$ ]  $\mu mol~m^{-2}~s^{-1}$  during the first and the second hour of the corrosion period, respectively. More rapid surface retreat begins with the combination of linear and non-linear distribution flux of [1.07  $\pm$  0.037]  $\mu mol~m^{-2}~s^{-1}$  at the next hour of the corrosion period and a new dissolution rate of [1.95  $\pm$  0.035]  $\mu$ mol m<sup>-2</sup> s<sup>-1</sup> toward the end of the experiment, verifying that the spatial distribution of rate contributors is not homogeneous. The in situ nanoscale experimental results also agreed in trend with the electrochemical information and chemical composition analysis, wherein increase Al concentrations are obtained in the solution as the material corrodes. Finally, the dissolution fluxes for all considered test methods follow a similar pattern during the corrosion experiment, with the least rates observed from the nanoscale SMI data. These results show the capability of applying the novel SMI for nanoscale characterization of corrosion. Thus, the presented method can be used as another in situ surface characterization method. The SMI-Electrochemical data from this study can provide the directly comparison of the influence of thermal history on Al alloy corrosion mode and help in building a better corrosion models for practical implications and applications in automotive corrosion engineering. Finally, future work seeks to conduct corrosion experiments occurring over long periods (i.e., hours to days) and be linked with the in situ nanoscale characterization of corrosion from SMI. The integration of multiple tests could provide more detailed quantitative and qualitative information on the corrosion initiation and propagation, as well as its mechanism, which is necessary to model the corrosion of alloys in the field.

# **Declaration of Competing Interest**

#### No

#### Acknowledgements

The authors wish to express their sincere appreciation to the insightful and constructive comments of anonymous reviewers. Funding is acknowledged through the Ford University Research Program.

### Appendix B. Supplementary data

The Supplementary Material is available for download at https://doi.org/10.1016/j.matchar.2022.111992 and includes Appendices A, B, and C.

#### References

- [1] R. Rodrigues, S. Gaboreau, J. Gance, I. Ignatiadis, S. Betelu, Reinforced concrete structures: a review of corrosion mechanisms and advances in electrical methods for corrosion monitoring, Constr. Build. Mater. (2020) 121240, https://doi.org/ 10.1016/j.conbuildmat.2020.121240.
- [2] C. Wang, Y. Cai, C. Ye, S. Dong, X. Cai, Y. Cao, C. Lin, In situ monitoring of the localized corrosion of 304 stainless steel in FeCl3 solution using a joint electrochemical noise and scanning reference electrode technique, Electrochem. Commun. 90 (2018) 11–15, https://doi.org/10.1016/j.elecom.2018.03.002.
- [3] B. Zhang, J. Wang, B. Wu, X.W. Guo, Y.J. Wang, D. Chen, Y.C. Zhang, K. Du, E. E. Oguzie, X.L. Ma, Unmasking chloride attack on the passive film of metals, Nat. Commun. 9 (2018) 1–9, https://doi.org/10.1038/s41467-018-04942-x.
- [4] J. Orlikowski, A. Jazdzewska, R. Mazur, K. Darowicki, Determination of pitting corrosion stage of stainless steel by galvanodynamic impedance spectroscopy, Electrochim. Acta 253 (2017) 403–412, https://doi.org/10.1016/j. electrota 2017 09 047
- [5] N.N. Khobragade, M.I. Khan, A.P. Patil, Corrosion behaviour of chrome-manganese austenitic stainless steels and AISI 304 stainless steel in chloride environment, Trans. Indian Inst. Metals 67 (2014) 263–273, https://doi. org/10.1007/s12666-013-0345-8.
- [6] T. Laitinen, Localized corrosion of stainless steel in chloride, sulfate and thiosulfate containing environments, Corros. Sci. 42 (2000) 421–441, https://doi.org/ 10.1016/j.msea.2004.06.041.
- [7] E.O. Fanijo, A.S. Brand, Anti-corrosion behaviors of corn-based polyols on low carbon steel rebar, Clean. Mater. (2022) 100066, https://doi.org/10.1016/j. clema 2022 100066
- [8] N.A. Mariano, D. Spinelli, Stress corrosion cracking of stainless steel used in drill collars, Mater. Sci. Eng. A 385 (2004) 212–219, https://doi.org/10.1016/j. msea.2004.06.041.
- [9] L. Wang, S. Chen, B. Yuan, F. Meng, J. Wang, C. Wang, L. Liang, Digital holographic reconstruction detection of localized corrosion arising from scratches, J. Serbian Chem. Soc. 75 (2010) 505–512, https://doi.org/10.2298/ JSC090627016W.
- [10] O. Pedram, E. Poursaeidi, R. Khamedi, H. Shayani-jam, Y. Mollapour, Development of an accelerated test for pitting corrosion of CUSTOM 450 by rDHM, Int. J. Mater. Res. 112 (2021) 600–609, https://doi.org/10.1515/jjmr-2020-7998.
- [11] Koch, M.P.H. Brongers, N.G. Thompson, Y.P. Virmani, J.H. Payer, Corrosion Cost and Preventive Strategies in the United States, Federal Highway Administration, United States, 2002.
- [12] S.R. Francia, J.C.Y. Llanos, Materials: corrosion, its tradition and scope, Rev. Del Inst. Investig. La Fac. Ing. Geológica, Minera, Met. y Geográfica. 6 (2003) 71–77, https://doi.org/10.15381/iigeo.v6i11.751.
- [13] G. Koch, J. Varney, N. Thompson, O. Moghissi, M. Gould, J. Payer, International Measures of Prevention, Application, and Economics of Corrosion Technologies Study, NACE International, Houston, TX, 2016.
- [14] G. Svenningsen, M.H. Larsen, J.C. Walmsley, J.H. Nordlien, K. Nisancioglu, Effect of artificial aging on intergranular corrosion of extruded AlMgSi alloy with small Cu content, Corros. Sci. 48 (2006) 1528–1543, https://doi.org/10.1016/j. corsci.2005.05.045.
- [15] D. Altenpohl, J.G. Kaufman, de la Source Aluminum-Technology, Applications, and Environment: A Profile of a Modern Metal: Aluminum from within-the Sixth Edition, distributeur Aluminum Association, Minerals, Metals & Materials Society, 2017
- [16] P.E. Fortin, M.J. Bull, D.M. Moore, An Optimized Aluminum Alloy (x6111) for Auto Body Sheet Applications, SAE Technical Paper 830096, 1983, https://doi. org/10.4271/830096.
- [17] B.G. Thomas, J.T. Parkman, T. Chandra, Thermec '97, Int. Conf. on Thermomechanical Processing of Steel and Other Materials 2, 1997, pp. 2279–2285.
- [18] A.K. Gupta, P.H. Marois, D.J. Lloyd, Study of the precipitation kinetics in a 6000 series automotive sheet material, in: Mater. Sci. Forum, Trans Tech Publ, 1996, pp. 801–808, https://doi.org/10.4028/www.scientific.net/MSF.217-222.801.
- [19] C. Vasilescu, S.I. Drob, P. Osiceanu, P. Drob, J.M.C. Moreno, S. Preda, S. Ivanescu, E. Vasilescu, Surface analysis, microstructural, mechanical and electrochemical properties of new Ti-15Ta-5Zr alloy, Met. Mater. Int. 21 (2015) 242–250, https://doi.org/10.1007/s12540-015-4074-x.
- [20] E. Poursaeidi, A.M. Niaei, M. Arablu, A. Salarvand, Experimental investigation on erosion performance and wear factors of custom 450 steel as the first row blade material of an axial compressor, Int. J. Surf. Sci. Eng. 11 (2017) 85–99.

- [21] O. Oudbashi, S.M. Emami, H. Ahmadi, P. Davami, Micro-stratigraphical investigation on corrosion layers in ancient bronze artefacts by scanning electron microscopy energy dispersive spectrometry and optical microscopy, Herit. Sci. 1 (2013) 1–10, https://doi.org/10.1186/2050-7445-1-21.
- [22] O. Oudbashi, Multianalytical study of corrosion layers in some archaeological copper alloy artefacts, Surf. Interface Anal. 47 (2015) 1133–1147, https://doi.org/ 10.1002/sia.5865
- [23] G. Fargas, M. Anglada, A. Mateo, Effect of the annealing temperature on the mechanical properties, formability and corrosion resistance of hot-rolled duplex stainless steel, J. Mater. Process. Technol. 209 (2009) 1770–1782, https://doi.org/ 10.1007/s00339-018-2007-5.
- [24] E. Poursaeidi, A.M. Niaei, M. Lashgari, K. Torkashvand, Experimental studies of erosion and corrosion interaction in an axial compressor first stage rotating blade material, Appl. Phys. A Mater. Sci. Process. 124 (2018) 1–15, https://doi.org/ 10.1016/j.imst.2019.01.013.
- [25] B. Zhang, X.L. Ma, A review—pitting corrosion initiation investigated by TEM, J. Mater. Sci. Technol. 35 (2019) 1455–1465, https://doi.org/10.1016/j. imst.2019.01.013.
- [26] A. Kosari, H. Zandbergen, F. Tichelaar, P. Visser, P. Taheri, H. Terryn, J.M.C. Mol, In-situ nanoscopic observations of dealloying-driven local corrosion from surface initiation to in-depth propagation, Corros. Sci. 177 (2020) 108912, https://doi. org/10.1016/j.corsci.2020.108912.
- [27] A. Kosari, F. Tichelaar, P. Visser, P. Taheri, H. Zandbergen, H. Terryn, J.M.C. Mol, Nanoscopic and in-situ cross-sectional observations of Li-based conversion coating formation using liquid-phase TEM, Npj Mater. Degrad. 5 (2021) 40, https://doi. org/10.1038/s41529-021-00189-y.
- [28] S.M. Ghahari, A.J. Davenport, T. Rayment, T. Suter, J.-P. Tinnes, C. Padovani, J. A. Hammons, M. Stampanoni, F. Marone, R. Mokso, In situ synchrotron X-ray micro-tomography study of pitting corrosion in stainless steel, Corros. Sci. 53 (2011) 2684–2687, https://doi.org/10.1016/j.corsci.2011.05.040.
- [29] R. Rizzo, S. Baier, M. Rogowska, R. Ambat, An electrochemical and X-ray computed tomography investigation of the effect of temperature on CO2 corrosion of 1Cr carbon steel, Corros. Sci. 166 (2020) 108471, https://doi.org/10.1016/j. corsci.2020.108471.
- [30] A.S.S. Singaravelu, J.J. Williams, H.D. Goyal, S. Niverty, S.S. Singh, T.J. Stannard, X. Xiao, N. Chawla, 3D time-resolved observations of fatigue crack initiation and growth from corrosion pits in Al 7XXX alloys using in situ synchrotron X-ray tomography, Metall. Mater. Trans. A. 51 (2020) 28–41, https://doi.org/10.1007/s11661.010.05510.7
- [31] F.A. Almuaili, S.A. McDonald, P.J. Withers, D.L. Engelberg, Application of a quasi in situ experimental approach to estimate 3-D pitting corrosion kinetics in stainless steel, J. Electrochem. Soc. 163 (2016) C745, https://doi.org/10.1149/ 2.0391613iee
- [32] H. Chen, Z. Qin, M. He, Y. Liu, Z. Wu, Application of electrochemical atomic force microscopy (EC-AFM) in the corrosion study of metallic materials, Materials (Basel) 13 (2020) 668. https://doi.org/10.3390/ma13030668.
- [33] K. Yasakau, Application of AFM-based techniques in studies of corrosion and corrosion inhibition of metallic alloys, Corros. Mater. Degrad. 1 (2020) 345–372, https://doi.org/10.3390/cmd1030017.
- [34] X. Shi, W. Qing, T. Marhaba, W. Zhang, Atomic force microscopy-scanning electrochemical microscopy (AFM-SECM) for nanoscale topographical and electrochemical characterization: principles, applications and perspectives, Electrochim. Acta 332 (2020) 135472, https://doi.org/10.1016/j. electacta.2019.135472.
- [35] B. Díaz-Benito, F. Velasco, S. Guzmán, R. Calabrés, AFM study of steel corrosion in aqueous solutions in concrete, Mater. Constr. 61 (2011) 27–37, https://doi.org/ 10.3989/mc.2010.59410.
- [36] J. Sánchez, J. Fullea, C. Andrade, J.J. Gaitero, A. Porro, AFM study of the early corrosion of a high strength steel in a diluted sodium chloride solution, Corros. Sci. 50 (2008) 1820–1824, https://doi.org/10.1016/j.corsci.2008.03.013.
- [37] A. Ma, L. Zhang, D. Engelberg, Q. Hu, S. Guan, Y. Zheng, Understanding crystallographic orientation dependent dissolution rates of 90Cu-10Ni alloy: new insights based on AFM/SKPFM measurements and coordination number/electronic structure calculations, Corros. Sci. 164 (2020) 108320, https://doi.org/10.1016/j. corsci.2019.108320.
- [38] P. Guo, E.C. La Plante, B. Wang, X. Chen, M. Balonis, M. Bauchy, G. Sant, Direct observation of pitting corrosion evolutions on carbon steel surfaces at the nano-tomicro- scales, Sci. Rep. 8 (2018) 7990, https://doi.org/10.1038/s41598-018-26340.5
- [39] J. Heuer, A. Luttge, Kinetics of pipeline steel corrosion studied by Raman spectroscopy-coupled vertical scanning interferometry, Npj Mater. Degrad. 2 (2018) 40, https://doi.org/10.1038/s41529-018-0061-2.
- [40] H. Torbati-Sarraf, T.J. Stannard, E.C. La Plante, G.N. Sant, N. Chawla, Direct observations of microstructure-resolved corrosion initiation in AA7075-T651 at the nanoscale using vertical scanning interferometry (VSI), Mater. Charact. 161 (2020) 110166, https://doi.org/10.1016/j.matchar.2020.110166.
- [41] Y. Pourvais, P. Asgari, P. Abdollahi, R. Khamedi, A.-R. Moradi, Microstructural surface characterization of stainless and plain carbon steel using digital holographic microscopy, J. Opt. Soc. Am. B 34 (2017) 36–41, https://doi.org/ 10.1364/JOSAB.34.000B36.
- [42] P. Asgari, Y. Pourvais, P. Abdollahi, A.R. Moradi, R. Khamedi, A. Darudi, Digital holographic microscopy as a new technique for quantitative measurement of microstructural corrosion in austenitic stainless steel, Mater. Des. 125 (2017) 109–115, https://doi.org/10.1016/j.matdes.2017.03.085.

- [43] L. Li, C. Wang, S. Chen, X. Yang, B. Yuan, H. Jia, An investigation on general corrosion and pitting of iron with the in-line digital holography, Electrochim. Acta 53 (2008) 3109–3119, https://doi.org/10.1016/j.electacta.2007.11.040.
- [44] B. Yuan, Z. Li, S. Tong, L. Li, C. Wang, In situ monitoring of pitting corrosion on stainless steel with digital holographic surface imaging, J. Electrochem. Soc. 166 (2019) C3039–C3047, https://doi.org/10.1149/2.0061911jes.
- [45] J.A.M. Salgado, D.M. Cruz, J.U. Chavarín, O.S. Martínez, Quantification of corrosion products formation onto a copper sample by digital holographic microscopy, Appl. Phys. Lett. 11 (2013) 77–79, https://doi.org/10.7149/ OPA. 46.1.49.
- [46] J. Jiang, Y. Liu, H. Chu, D. Wang, H. Ma, W. Sun, Pitting corrosion behaviour of new corrosion-resistant reinforcement bars in chloride-containing concrete pore solution, Materials (Basel) 10 (2017) 903, https://doi.org/10.3390/ma10080903.
- [47] Y. Hu, X. Li, Z. Jiao, G. Gao, B. Yuan, L. Li, C. Wang, Investigation into the anodic dissolution processes of copper in neutral and acidic sulfate solutions with the inline digital holography, Electrochemistry 84 (2016) 378–382, https://doi.org/ 10.5796/electrochemistry.84.378.
- [48] M. Zhang, B. Yuan, Q. Wu, Y. Zhu, L. Li, C. Wang, Study of the effects of the magnetic field on the anodic dissolution of nickel with in-line digital holography, Int. J. Electrochem. Sci. 13 (2018) 739–751, https://doi.org/10.20964/ 2018.01.46.
- [49] M.K. Kim, Digital Holographic Microscopy, Springer, N. Y., 2011, https://doi.org/ 10.1007/978-1-4419-7793-9.
- [50] M. Mir, B. Bhaduri, R. Wang, R. Zhu, G. Popescu, Quantitative phase imaging, in: E. Wolf (Ed.), Prog. Opt., Elsevier, 2012, pp. 133–217, https://doi.org/10.1016/ B978-0-44-459422-8 00003-5
- [51] A. Luttge, R.S. Arvidson, Reactions at surfaces: a new approach integrating interferometry and kinetic simulations, J. Am. Ceram. Soc. 93 (2010) 3519–3530, https://doi.org/10.1111/j.1551-2916.2010.04141.x.
- [52] C. Fischer, R.S. Arvidson, A. Lüttge, How predictable are dissolution rates of crystalline material? Geochim. Cosmochim. Acta 98 (2012) 177–185, https://doi. org/10.1016/j.gca.2012.09.011.
- [53] C. Fischer, I. Kurganskaya, T. Schäfer, A. Lüttge, Variability of crystal surface reactivity: what do we know? Appl. Geochem. 43 (2014) 132–157, https://doi. org/10.1016/j.apgeochem.2014.02.002.
- [54] C. Fischer, A. Luttge, Beyond the conventional understanding of water-rock reactivity, Earth Planet. Sci. Lett. 457 (2017) 100–105, https://doi.org/10.1016/j. epsl.2016.10.019.
- [55] I. Bibi, R.S. Arvidson, C. Fischer, A. Lüttge, Temporal evolution of calcite surface dissolution kinetics, Minerals 8 (2018) 256, https://doi.org/10.3390/ min8060256.
- [56] C. Fischer, A. Luttge, Pulsating dissolution of crystalline matter, Proc. Natl. Acad. Sci. 115 (2018) 897–902, https://doi.org/10.1073/pnas.1711254115.
- [57] C. Fischer, I. Kurganskaya, A. Luttge, Inherited control of crystal surface reactivity, Appl. Geochem. 91 (2018) 140–148, https://doi.org/10.1016/j. apgeochem.2018.02.003.
- [58] E.T. Pedrosa, I. Kurganskaya, C. Fischer, A. Luttge, A statistical approach for analysis of dissolution rates including surface morphology, Minerals 9 (2019) 458, https://doi.org/10.3390/min9080458.
- [59] X. Li, Q. Wang, X. Shen, E.T. Pedrosa, A. Luttge, Multiscale investigation of olivine (010) face dissolution from a surface control perspective, Appl. Surf. Sci. 549 (2021) 149317, https://doi.org/10.1016/j.apsusc.2021.149317.
- [60] T. Bollermann, C. Fischer, Temporal evolution of dissolution kinetics of polycrystalline calcite, Am. J. Sci. 320 (2020) 53–71, https://doi.org/10.2475/ 21.2020.044
- [61] P. Agrawal, T. Bollermann, A. Raoof, O. Iliev, C. Fischer, M. Wolthers, The contribution of hydrodynamic processes to calcite dissolution rates and rate spectra, Geochim. Cosmochim. Acta 307 (2021) 338–350, https://doi.org/ 10.1016/j.gca.2021.05.003.
- [62] A.S. Brand, P. Feng, J.W. Bullard, Calcite dissolution rate spectra measured by in situ digital holographic microscopy, Geochim. Cosmochim. Acta 213 (2017) 317–329, https://doi.org/10.1016/j.gca.2017.07.001.
- [63] P. Feng, A.S. Brand, L. Chen, J.W. Bullard, In situ nanoscale observations of gypsum dissolution by digital holographic microscopy, Chem. Geol. 460 (2017) 25–36, https://doi.org/10.1016/j.chemgeo.2017.04.008.
- [64] A.S. Brand, J.W. Bullard, Dissolution kinetics of cubic tricalcium aluminate measured by digital holographic microscopy, Langmuir 33 (2017) 9645–9656, https://doi.org/10.1021/acs.langmuir.7b02400.
- [65] A.S. Brand, S.B. Feldman, P.E. Stutzman, A.V. Ievlev, M. Lorenz, D.C. Pagan, S. Nair, J.M. Gorham, J.W. Bullard, Dissolution and initial hydration behavior of tricalcium aluminate in low activity sulfate solutions, Cem. Concr. Res. 130 (2020) 105989, https://doi.org/10.1016/j.cemconres.2020.105989.
- [66] A.S. Brand, J.M. Gorham, J.W. Bullard, Dissolution rate spectra of  $\beta$ -dicalcium silicate in water of varying activity, Cem. Concr. Res. 118 (2019) 69–83, https://doi.org/10.1016/j.cemconres.2019.02.014.
- [67] S. Ye, P. Feng, Y. Liu, J. Liu, J.W. Bullard, In situ nano-scale observation of C<sub>3</sub>A dissolution in water, Cem. Concr. Res. 132 (2020) 106044, https://doi.org/10.1016/j.cemconres.2020.106044.
- [68] S. Ye, P. Feng, Y. Liu, J. Liu, J.W. Bullard, Dissolution and early hydration of tricalcium aluminate in aqueous sulfate solutions, Cem. Concr. Res. 137 (2020) 106191, https://doi.org/10.1016/j.cemconres.2020.106191.
- [69] A.P. Abbott, M. Azam, K.S. Ryder, S. Saleem, In situ electrochemical digital holographic microscopy; a study of metal electrodeposition in deep eutectic solvents, Anal. Chem. 85 (2013) 6653–6660, https://doi.org/10.1021/ac400262c.
- [70] V. Brasiliense, P. Berto, C. Combellas, G. Tessier, F. Kanoufi, Electrochemistry of single nanodomains revealed by three-dimensional holographic microscopy, Acc.

- Chem. Res. 49 (2016) 2049–2057, https://doi.org/10.1021/acs.
- [71] A. Lalisse, A. Al Mohtar, M.C. Nguyen, R. Carminati, J. Plain, G. Tessier, Quantitative temperature measurements in gold nanorods using digital holography, ACS Appl. Mater. Interfaces 13 (2021) 10313–10320, https://doi.org/ 10.1021/accami.0c.22420
- [72] B. Yuan, C. Wang, L. Li, S. Chen, Real time observation of the anodic dissolution of copper in NaCl solution with the digital holography, Electrochem. Commun. 11 (2009) 1373–1376, https://doi.org/10.1016/j.elecom.2009.05.008.
- [73] G. Gao, B. Yuan, C. Wang, L. Li, S. Chen, The anodic dissolution processes of copper in sodium fluoride solution, Int. J. Electrochem. Sci. 9 (2014) 2565–2574.
- [74] E. Fanijo, A. Brand. Initiation of Chloride-Induced Corrosion of Low Carbon Steel Rebar in Concrete Using In-situ Quantitative Phase Microscopy, 2021.
- [75] S. Dong, X. Chen, E.C. La Plante, M. Gussev, K. Leonard, G. Sant, Elucidating the grain-orientation dependent corrosion rates of austenitic stainless steels, Mater. Des. 191 (2020) 108583, https://doi.org/10.1016/j.matdes.2020.108583.
- [76] E.Q. Contreras, J. Huang, R.S. Posusta, D.K. Sharma, C. Yan, P. Guraieb, M. B. Tomson, R.C. Tomson, Optical measurement of uniform and localized corrosion of C1018, SS 410, and Inconel 825 alloys using white light interferometry, Corros. Sci. 87 (2014) 383–391, https://doi.org/10.1016/j.corsci.2014.06.046.
- [77] J. Jiang, H. Chu, Y. Liu, D. Wang, D. Guo, W. Sun, Galvanic corrosion of duplex corrosion-resistant steel rebars under carbonated concrete conditions, RSC Adv. 8 (2018) 16626–16635, https://doi.org/10.1039/C8RA03320J.
- [78] R. Shang, S. Chen, C. Li, Y. Zhu, Spectral modulation interferometry for quantitative phase imaging, Biomed. Opt. Express 6 (2015) 473, https://doi.org/ 10.1364/BOE.6.000473.
- [79] L.G. Hector, Y.-L. Chen, S. Agarwal, C.L. Briant, Texture characterization of autogenous Nd: YAG laser welds in AA5182-O and AA6111-T4 aluminum alloys, Metall. Mater. Trans. A. 35 (2004) 3032–3038.
- [80] G.J. Tearney, R.H. Webb, B.E. Bouma, Spectrally encoded confocal microscopy, Opt. Lett. 23 (1998) 1152–1154, https://doi.org/10.1364/OL.23.001152.
- [81] D. Yelin, W.M. White, J.T. Motz, S.H. Yun, B.E. Bouma, G.J. Tearney, Spectral-domain spectrally-encoded endoscopy, Opt. Express 15 (2007) 2432–2444, https://doi.org/10.1364/OE.15.002432.
- [82] L. Froehly, S.N. Martin, T. Lasser, C. Depeursinge, F. Lang, Multiplexed 3D imaging using wavelength encoded spectral interferometry: a proof of principle, Opt. Commun. 222 (2003) 127–136, https://doi.org/10.1016/S0030-4018(03)01611-0
- [83] L. Golan, D. Yeheskely-Hayon, L. Minai, D. Yelin, High-speed interferometric spectrally encoded flow cytometry, Opt. Lett. 37 (2012) 5154–5156, https://doi. org/10.1364/OL.37.005154.
- [84] A.S. Brand, Phase uncertainty in digital holographic microscopy measurements in the presence of solution flow conditions, J. Res. Natl. Inst. Stand. Technol. 122 (022) (2017) 1–41, https://doi.org/10.6028/jres.122.022.

- [85] K. Kletetschka, J.D. Rimstidt, T.E. Long, F.M. Michel, Suitability of 3D-printed devices for low-temperature geochemical experiments, Appl. Geochem. 98 (2018) 121–126, https://doi.org/10.1016/j.apgeochem.2018.08.012.
- [86] F.M. Michel, J.D. Rimstidt, K. Kletetschka, 3D printed mixed flow reactor for geochemical rate measurements, Appl. Geochem. 89 (2018) 86–91, https://doi. org/10.1016/j.apgeochem.2017.11.008.
- [87] W. APHA AWWA, Standard Methods for the Examination of Water and Wastewater 20th Edition, Am. Public Heal. Assoc. Am. Water Work Assoc. Water Environ. Fed, Washington, DC, 1998.
- [88] K.D. Ralston, N. Birbilis, M.K. Cavanaugh, M. Weyland, B.C. Muddle, R.K. W. Marceau, Role of nanostructure in pitting of Al-Cu-Mg alloys, Electrochim. Acta 55 (2010) 7834–7842, https://doi.org/10.1016/j.electacta.2010.02.001.
- [89] K. Ogle, S. Weber, Anodic dissolution of 304 stainless steel using atomic emission spectroelectrochemistry, J. Electrochem. Soc. 147 (2000) 1770–1780, https://doi. org/10.1149/1.1393433.
- [90] K. Ogle, Atomic emission spectroelectrochemistry: Real-time rate measurements of dissolution, corrosion, and passivation, Corrosion 75 (2019) 1398–1419, https://doi.org/10.5006/3336.
- [91] J.G. Brunner, N. Birbilis, K.D. Ralston, S. Virtanen, Impact of ultrafine-grained microstructure on the corrosion of aluminium alloy AA2024, Corros. Sci. 57 (2012) 209–214, https://doi.org/10.1016/j.corsci.2011.12.016.
- [92] O. Gharbi, D. Jiang, D.R. Feenstra, S.K. Kairy, Y. Wu, C.R. Hutchinson, N. Birbilis, On the corrosion of additively manufactured aluminium alloy AA2024 prepared by selective laser melting, Corros. Sci. 143 (2018) 93–106, https://doi.org/10.1016/j. corsci.2018.08.019.
- [93] N. Homazava, A. Ulrich, M. Trottmann, U. Krähenbühl, Micro-capillary system coupled to ICP-MS as a novel technique for investigation of micro-corrosion processes, J. Anal. At. Spectrom. 22 (2007) 1122–1130, https://doi.org/10.1039/ R705.248K
- [94] T. Hashimoto, X. Zhang, X. Zhou, P. Skeldon, S.J. Haigh, G.E. Thompson, Investigation of dealloying of S phase (Al2CuMg) in AA 2024-T3 aluminium alloy using high resolution 2D and 3D electron imaging, Corros. Sci. 103 (2016) 157-164, https://doi.org/10.1016/j.corsci.2015.11.013.
- [95] X. Zhang, X. Zhou, T. Hashimoto, B. Liu, Localized corrosion in AA2024-T351 aluminium alloy: transition from intergranular corrosion to crystallographic pitting, Mater. Charact. 130 (2017) 230–236, https://doi.org/10.1016/j. matchar.2017.06.022.
- [96] B. Gutmann, H. Weber, Phase unwrapping with the branch-cut method: role of phase-field direction, Appl. Opt. 39 (2000) 4802–4816, https://doi.org/10.1364/ AO.39.004802.
- [97] C. Fischer, S. Finkeldei, F. Brandt, D. Bosbach, A. Luttge, Direct measurement of surface dissolution rates in potential nuclear waste forms: the example of pyrochlore, ACS Appl. Mater. Interfaces 7 (2015) 17857–17865, https://doi.org/ 10.1021/acsami.5b04281.